

# Identifying high Alpine Geomorphological processes using Permanent Terrestrial Laser Scanning time series

Paco Frantzen





# Identifying high Alpine Geomorphological processes using Permanent Terrestrial Laser Scanning time series

Master Thesis

by

Paco Frantzen

To obtain the degree of  
Master of Science in Civil Engineering (Geoscience and Remote Sensing)  
at the Delft University of Technology.

Graduation Supervisor:	R. C. Lindenbergh	Delft University of Technology
Research Supervisor:	M. Rutzinger	Universität Innsbruck
Additional supervisor:	A. B. Voordendag	Universität Innsbruck
Additional supervisor:	M. Kuschnerus	Delft University of Technology
Additional supervisor:	B. Wouters	Delft University of Technology
Institution:	Delft University of Technology	
Faculty:	Civil Engineering and Geosciences	
Master track:	Geoscience and Remote Sensing	
Project Duration:	March, 2022 - December, 2022	

Cover Image: Photo of the Im Hinteren Eis laser scanner housing with the Hintereisferner and Hochvernaglwand in the background, captured during a visit to the scanning system on 3 June 2022.



# Abstract

Global climate change affects mountain regions such as the European Alps. Consequently, glacier extents decrease, and proglacial areas, the areas that recently lost their ice cover, increase in size. These proglacial areas are subject to a high frequency and magnitude of geomorphological activity and act as a sediment source for downstream fluvial systems, extending the influence of their activity beyond proglacial margins. Therefore, a good understanding of the geomorphological activity in these regions is important and subject to numerous studies. Challenges to access Alpine proglacial areas complicate collection of data with high spatial and temporal coverage. A permanently installed terrestrial laser scanner (TLS) overlooking the Hintereisferner glacier in the Ötztaler Alps (Austria) provides daily ranging observations of a proglacial area. The aim of this study is to assess the potential of this permanent laser scanning system for identifying geomorphological processes in proglacial areas. Point clouds of this TLS system were rasterised into range images. An automated registration method is developed to ensure alignment of large quantities of range images in the event of scanner movement. Scans of the 2020 and 2022 summer were combined into two 4D spatiotemporal datasets, allowing analysis of range change time series for each raster cell. A principal component analysis (PCA) of the 4D spatiotemporal datasets is used to explore spatial and temporal patterns of change in the observed proglacial area. The range image registration procedure performed slightly worse than conventional registration methods, but allowed for automated registration of large quantities of scans. Based on the patterns found in the PCA, as well as in the range time series and precipitation data, different geomorphological processes are identified in the observed proglacial area at daily time scales, with magnitudes of several meters. Among these processes are debris flows in gullies, and slumps on lateral moraines. These results demonstrate that characteristic patterns of topographical change can be distinguished using PCA, and PCA is a promising method to be used in other studies exploiting 4D spatiotemporal datasets. The identification of different geomorphological processes indicates that the permanent TLS system could be of use for further research on geomorphological activity in proglacial areas, such as reworking of lateral moraines, while the developed methodology could be used in other studies exploring 4D spatiotemporal datasets as well.



# Preface

This thesis is my final project for the master Geoscience and Remote Sensing, and hence, my education at the Delft University of Technology. For this project, I did my research at the Remote Sensing and Topographic LiDAR Research Group of the Universität Innsbruck in Austria, from April until October 2022.

Having always visited the mountains during holidays, I was excited when provided with the opportunity to research, and temporarily live in the Austrian Alps for this project. Doing so provided me with great experiences in the mountains that I could not have acquired during a holiday. I am grateful to Roderik and Martin for providing me with the opportunity to work on this project at the Universität Innsbruck and to participate in the 2022 Innsbruck Summer School of Alpine Research. This topic kept me interested and highly motivated throughout the duration of the thesis project because so many of my interests were involved. Furthermore I would like to thank Martin, Annelies, Betty, Andreas, Magnus, Lotte, Klaus, and many other academics at the Universität Innsbruck for the great time I had while doing my research. You provided me with nice discussions, entertaining lunch breaks, and helpful tips regarding life in Innsbruck. I would also like to thank Rainer for allowing me to join a trip to the scanning instrument, during which I learned a lot about life in Tyrol, and the research performed by Universität Innsbruck.

During my thesis project I had the pleasure to be supervised by Roderik, Martin, Mieke and Annelies, whom I thank for the valuable discussions and suggestions on my work during our meetings. Additionally I would like to thank Bert for his contributions and feedback as a committee member.

Besides my study activities, I had a great time during the thesis project, for which I would like to thank my friends in Innsbruck, for their hospitality and the fun we had in the city and the mountains. Finally, I would like to thank my friends and family for their support and kindness during my studies.

*Paco Frantzen  
Delft, December 2022*



# Contents

<b>1</b>	<b>Introduction</b>	<b>1</b>
<b>2</b>	<b>Background</b>	<b>3</b>
2.1	Geomorphological processes in high alpine slopes . . . . .	3
2.2	Monitoring geomorphological change . . . . .	4
2.2.1	LiDAR monitoring techniques . . . . .	5
2.2.2	Registration of LiDAR data . . . . .	6
2.3	Principal component analysis . . . . .	7
2.4	Related work . . . . .	7
<b>3</b>	<b>Data description</b>	<b>8</b>
3.1	Instrument . . . . .	8
3.2	Errors and uncertainties . . . . .	11
3.3	Area of interest . . . . .	12
<b>4</b>	<b>Methodology</b>	<b>14</b>
4.1	Workflow overview . . . . .	14
4.2	Stable area identification . . . . .	14
4.2.1	Point cloud registration . . . . .	15
4.2.2	reference zones for registration procedure . . . . .	16
4.3	Creating 4D spatiotemporal data set . . . . .	17
4.3.1	Overview of steps . . . . .	17
4.3.2	Conversion to range images . . . . .	18
4.3.3	Range Image registration . . . . .	20
4.3.4	Time series creation . . . . .	26
4.4	Low variation areas . . . . .	26
4.5	Principal component analysis . . . . .	27
<b>5</b>	<b>Results</b>	<b>30</b>
5.1	Range image registration . . . . .	30
5.2	Identification of geomorphological processes . . . . .	33
5.2.1	Example cases . . . . .	34
5.2.2	Small magnitude change . . . . .	37
5.2.3	Principal components . . . . .	38
<b>6</b>	<b>Discussion</b>	<b>46</b>
6.1	Range image registration . . . . .	46
6.2	Time series creation and examples . . . . .	48
6.3	Small magnitude change . . . . .	48
6.4	Principal component analysis . . . . .	49
6.5	Potential of the IHE laser scanner for observing geomorphological processes . . . . .	51
<b>7</b>	<b>Conclusions and recommendations</b>	<b>53</b>
7.1	Conclusions . . . . .	53
7.2	Recommendations . . . . .	54
	<b>Bibliography</b>	<b>58</b>

# 1

## Introduction

Alpine glaciers decrease in size since the little ice age in the mid-19th century (Heckmann et al., 2019). Paired with the disappearance of ice, in high alpine environments, more rock slopes and sediment get uncovered. These newly exposed features are not always stable and different phenomena can cause topographical changes (S. McColl et al., 2019), such as rockfall events (Fischer et al., 2006) and sediment transport (Curry et al., 2006).

Topographical change in high alpine environments has previously been mapped using techniques such as airborne laser scanning (ALS) (Sailer et al., 2014) or repeated terrestrial laser scanning (TLS) surveys (Vehling et al., 2017). Due to the involved costs and effort of these surveys, a limited amount of studies investigate topographical change on a sub seasonal scale using these techniques.

The introduction of the permanent terrestrial laser scanning (PLS) setup, allows large amounts of laser scans to be performed utilizing an automated observation setup. Thus, allowing studies of topographical change to be performed with multiple observations per day, over long time spans. With the intention of observing snow redistribution on the Hintereisferner (HEF) glacier, a PLS setup is installed at the Im Hinteren Eis (IHE) in the Ötztaler Alps, Austria. Besides the HEF, also the rock slopes adjacent to this glacier are within view of the laser scanner, thus providing a large series of repeated observations of a proglacial area subject to different geomorphological processes.

The aim of this research is to identify the different processes driving topographical change in the proglacial area adjacent to the HEF using the daily repeated LiDAR observations performed by the permanent laser scanning setup. The main research question of this research is: *How to identify high alpine geomorphological processes using long range permanent laser scanning?*

Sub-questions following this main research question are:

### **Which geomorphological processes can be distinguished using the PLS setup?**

Different geomorphological processes occur in the area of interest. To investigate how these processes could be identified using the PLS system, an overview of geomorphological processes should be created.

### **At what (spatio-temporal) scales can geomorphological processes be identified?**

Geomorphological processes occur at different temporal and spatial scales. The observation frequency, spatial resolution and other properties of the PLS system confine the range of geomorphological processes that may be identified.

### **How can uncertainty assessment of PLS data be incorporated in the identification of geomorphological processes?**

The observations of the PLS setup contain errors and uncertainties. It is important to deal with these uncertainties in a way that mitigates interpretation of these signals as topographical change. Therefore, it should be investigated how to identify errors, and how the influence of these errors could be limited.

**How can multiple observations be combined to decrease the limit of detection and detect smaller surface changes?**

The influence of random errors is possibly reduced through combining a large number of observations. A method should be identified which implements this concept in a way that fits the data.

**How can range images be used to analyse surface change?**

Analysis of topographical change is traditionally performed using point clouds or digital elevation models. Since the PLS setup results in observations of constant viewing position and orientation, it is interesting to research the use of range images as opposed to the aforementioned formats.

In the second chapter of this thesis, an overview is provided on different relevant topics of this thesis, including geomorphological processes, laser scanning, principal component analysis, and related works are discussed. Next, in chapter 3, a description of the available data and the PLS system is provided. In chapter 4, the methods used to identify geomorphological change using data from the used permanent laser scanning setup are presented. Chapter 5 provides the results of this research. In chapter 6, The methods and results are further discussed. Finally, in chapter 7, the conclusions as well as recommendations following this research are presented.

# 2

## Background

High elevation landscapes in the European Alps are characterized by the presence of glaciers and permafrost. Atmospheric warming causes changes in (sub)surface frost and ice (S. McColl et al., 2019). Due to atmospheric warming, glacier mass has been declining on a global scale in recent decades, and this decline is projected to continue for the following century (Pörtner et al., 2019). Reductions in glacier ice mass cause both glacier thinning, and retreat (Heckmann et al., 2019). The thinning and retreat of glaciers causes rock slopes to lose their ice cover, and the stability of rock slopes is lowered due to the removal of lateral ice support, also known as glacial debuttressing (S. McColl et al., 2019). During the glaciated state, rock slopes have endured glacial erosion, which can cause steepening of rock slopes (S. T. McColl et al., 2013). These steepened rock slopes may be subject to progressive strength degradation after exposure due to glacial mass loss (S. McColl et al., 2019). Processes of sediment release, storage, and redistribution also occur in deglaciating environments (Porter et al., 2019). features of substantial storage of glacial sediment are lateral moraines, which have the potential of being reworked and redistributed due to deglaciation (Porter et al., 2019).

Recently deglaciating areas, undergoing a transition from glaciated to a non-glaciated state are referred to as proglacial regions (Heckmann et al., 2019). These regions are sensitive to climate change and thermal effects affect slope stability at a range of temporal scales (S. McColl et al., 2019). The snow, ice, and rock are subject to heat fluxes due to temperature differences (S. McColl et al., 2019). Expansion and contraction of rock due to thermal changes can prepare or trigger rockfalls (Collins et al., 2016). Changes in temperature on a daily scale affect rock slope stability up to 0.5 m depth (S. McColl et al., 2019), which may trigger rockfall events. On a seasonal scale, thermal change may influence rock slopes at greater depths (Gischig et al., 2011).

Because ice within rock slopes acts as a factor increasing the shear resistance of slopes, rock slope stability is also influenced by the freeze and thaw of ice (S. McColl et al., 2019). Last, rising temperatures in permafrost regions are found to decrease rock slope stability (Fischer et al., 2006).

In this chapter, the geomorphological processes caused by the aforementioned conditions are presented in Section 2.1. Next, monitoring techniques used to record geomorphological processes are discussed in Section 2.2. Finally, applications for the statistical method of principal component analysis are presented in Section 2.3.

### **2.1. Geomorphological processes in high alpine slopes**

Proglacial regions are subject to numerous paraglacial processes which shape the landscape since the end of the little ice age (LIA) (Heckmann et al., 2019). An example proglacial area is shown in Figure 2.1 through a shaded relief representation. The intensity of geomorphological activity in proglacial areas differs from other high alpine rock slopes (Carrivick et al., 2017). Lateral moraines present in proglacial areas may act as a source and store of unconsolidated material (Porter et al., 2019). The reworking and modification of these features often occur episodically, caused by, for instance, precipitation events or dead ice body melting (Porter et al., 2019). processes of reworking due to the thaw of underlying

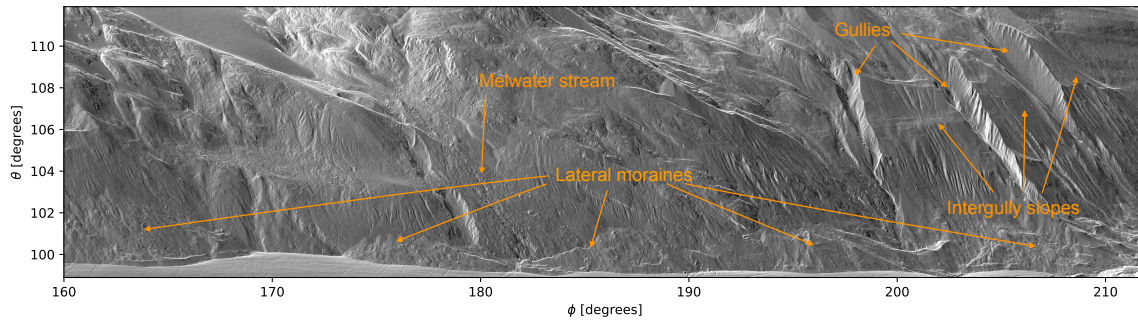


**Figure 2.1:** Shaded relief image of the proglacial area analysed in this thesis. Different geomorphological features such as gullies and lateral moraines are indicated.

ice include rapid failures in the form of slumping, and debris flows (Ballantyne, 2002). Steep lateral moraines are also reworked by fluvial erosion as well as slope wash and meltwater streams (Heckmann et al., 2019). These processes result in landscapes of gullied lateral moraines and valley sides, debris cones and fans, as well as valley floor deposits (Porter et al., 2019). Due to glacial debuttressing, rock slopes may slowly deform through rock mass creep (Ballantyne, 2002). Proglacial rock slopes may act as a source of unconsolidated material through rockfall, induced by rock slope instability (S. McColl et al., 2019, Knoflach et al., 2021). The resulting rockfall may be deposited on rock slopes, such that these slopes also function as a store for sediments. Reworking of sediment mantled slopes rock slopes is largely caused by debris flows (Ballantyne, 2002) resulting in the formation of gullies and downslope fans (Curry et al., 2006). Extreme rainfall events also contribute to sediment release from hill slopes (Porter et al., 2019). Proglacial streams may also erode rock slopes, and decrease the stability of rock slopes through undercutting (Porter et al., 2019). Furthermore, meltwater streams may also modify moraines (Porter et al., 2019).

## 2.2. Monitoring geomorphological change

Research on the geomorphological change of rock slopes can be performed at a large range of scales in both space and time. Therefore, different techniques exist for the monitoring of geomorphological change. To measure topographical change, in situ measurement techniques exist (S. McColl et al., 2019). A disadvantage of these techniques is the low amount of data collected, compared to the labour intensity of performing the measurements. A method of measuring topographical change which is more beneficial in terms of labour intensity and data quantity is through remote sensing techniques. In this section, two remote sensing techniques are presented. First, structure from motion photogrammetry is discussed. Next, LiDAR, is treated, which will be further discussed in more detail in Section 2.2.1.

### Structure from motion photogrammetry

Photogrammetry allows the creation of a digital 3D reconstruction of objects through collections of photographs. By identifying corresponding points in a set of photographs obtained from different positions, a digital 3D surface reconstruction similar to that resulting from LiDAR measurements can be obtained. A disadvantage of this technique is the fact that points must be visible in photographs taken from multiple locations to obtain their corresponding 3D representation. Furthermore, photography is a passive sensor technique. Thus, a light source illuminating the objects of interest is needed. A benefit of photogrammetry is the possibility of performing this technique using historical or crowd-sourced collections of images, allowing one to create 3D reconstructions, such as performed in (Altmann et al., 2020) and (Guerin et al., 2017) respectively.

In structure from motion photogrammetry, the position and orientation of the camera corresponding to the used photographs is not known. Thus, besides estimating a 3D representation of the observed objects, also the camera characteristics, positions, and orientations corresponding to each photograph must be estimated (Westoby et al., 2012). Camera characteristics that are to be estimated are the so-called intrinsic parameters, which describe the relation between the 3D coordinates of a point to its 2D representation in the camera image plane. The most widely used method of obtaining matchable

features from images is through the Scale Invariant Feature Transform (SIFT) algorithm (Smith et al., 2016). This algorithm detects features using a number of convolution operations. After features are computed for each image, features describing the same point between different images are identified. These so-called feature matches, along with the corresponding key point locations of the features are then used to estimate the different camera intrinsic parameters, positions, and orientations as well as the feature locations in a single reference frame.

## **LiDAR**

Light Detection And Ranging (LiDAR), also often referred to as laser scanning, is a non-contact active measurement technique that allows the recording of the geometry of visible surfaces of objects, resulting in a digital 3D representation of the scanned objects (Vosselman et al., 2010). To perform measurements, the instruments send out a laser pulse in a given direction and record the time of flight until a reflection of the pulse is observed. Using the assumed propagation speed of the laser pulse through the air, the range between the instrument and the reflecting object can be determined. By performing this action in many directions, a 3D representation of the surrounding of the instrument is obtained, expressed in coordinates relative to the instrument's position. A broader overview of monitoring techniques using LiDAR instruments is provided in Section 2.2.1. LiDAR measurements can be deployed through airborne and terrestrial systems such as UAVs, aircraft, helicopters, cars handheld devices, and tripods. This measurement technique can record the geometry of objects with an accuracy in the centimeter to decimeter range. Good spatial coverage can be achieved, especially if measurements are performed from different positions. A disadvantage of this technique is that in most ways this technique is used, quite some effort is needed to perform a single scan, and therefore monitoring geomorphological change using LiDAR is often with a small number of repeated measurements.

### **2.2.1. LiDAR monitoring techniques**

LiDAR or laser scanning is an observation technique that is used in a wide range of applications. The use of LiDAR in studies of topographical change is widespread and LiDAR instruments have been used in numerous setups. In this section, three laser scanning observation setups relevant to mapping topographical change are presented.

#### **Airborne Laser scanning**

In Airborne laser scanning (ALS), a laser scanner is attached to an aerial vehicle, which changes the scanner's position and orientation while acquiring data. As a result of this movement, Areas up to multiple square kilometers can be covered with a short observation distance, allowing this large area to be captured with a high spatial resolution. To express all laser scanning observations in a single reference frame, the position and orientation of the scanner must continuously be known during the scanning time. In order to obtain these parameters, ALS systems make use of high-precision GNSS positioning, as well as observations of the ALS system orientation through the use of an inertial measurement unit (IMU). This technique is used to quantify high alpine geomorphological processes (Bollmann et al., 2011, Sailer et al., 2014). Different types of aircraft can be used in ALS, such as airplanes, UAVs, and helicopters. A disadvantage of this technique is the uncertainties involved with the GNSS and IMU systems. To reduce errors in the final data, elaborate flight planning and post-processing are required. To estimate quality, a comparison is can be made to ground truth data of known flat surfaces (Vosselman et al., 2010).

#### **Terrestrial laser scanning**

In a TLS setup, a laser scanning instrument is attached to a tripod, and scanning can be performed in any direction besides the areas occluded by the scanner and tripod setup (Vosselman et al., 2010). Because laser scanning quality decreases with increasing angle of incidence to the reflecting surface (Lato et al., 2015), and TLS observations can be performed from multiple positions and orientations within an area of interest, TLS measurements can result in higher data quality than ALS for regions with complex or high slope angle topography. Furthermore, due to the shorter possible distances to the scanned surfaces compared to ALS, it is possible to measure surfaces with a higher point spacing using TLS. Because of the static setup, positioning can be performed with higher accuracy than in the case of ALS. A limitation of this measurement technique is the fact that the observations must be performed from the ground, which results in occlusions of horizontal fractures and bad data quality for horizontal

areas at instrument height (Lato et al., 2015). Furthermore, it is not always possible to observe an area of interest from multiple ground points because of limited accessibility. Draebing (Draebing et al., 2022) identified rock fall events in a paraglacial rock slope using repeated TLS observations.

### **Permanent laser scanning**

When a large number of repeated observations are desired, the cost and time involved with each repeated measurement are factors that might limit the number of repeated observations. A Permanent Laser Scanning (PLS) setup allows one to obtain a large number of repeated measurements over large time spans with little extra cost and operations per repeated observation. In this setup, scans are performed automatically, and the laser scanner is mounted to a rigid object to minimize changes in the scanner position and orientation over time. Thus the PLS system is permanent both spatially and temporally due to the possibility of near-continuous observations (Vos et al., 2022). Besides a TLS instrument, the operation of a PLS setup requires a power supply, a means of data transfer, a remote connection, and a stable instrument temperature. Therefore, a PLS setup cannot be installed at any location. Although this technique is relatively new, it is already applied in different setups. In (Vos et al., 2022), coastal topography in Kijkduijn is obtained hourly with a millimeter range accuracy using a PLS setup. To estimate the magnitude-frequency distribution of rockfall events at a coastal cliff, in (Williams et al., 2018), hourly observations from a permanently installed laser scanner were used. The mounting of the instruments in PLS setups is not perfectly stable (Voordendag et al., 2022, Kuschnerus et al., 2021a), resulting in possible misalignments in the resulting data. Therefore, registration of observations from PLS setups may still be required.

### **2.2.2. Registration of LiDAR data**

The positions of measured points are measured in the internally defined sensor reference frame of a TLS instrument (Vosselman et al., 2010). If a scanner changes its position or orientation between subsequent acquisitions, the different scans must be registered to a single coordinate system. This system could be for instance a local-level system or the coordinate system of one of the different scans. Different methods exist to estimate the parameters of a rigid transformation needed to express scans in a single coordinate system. A divide can be made into methods using ground control points and point-based methods.

#### **Ground control points based methods**

A common technique for point cloud registration using ground control points involves the use of laser scan targets. These planar targets contain a high contrast between components to create higher accuracy estimates of the target center (Vosselman et al., 2010). By including at least three stationary targets in each laser scan, the parameters of the rigid body transformation of different laser scan acquisitions can be estimated based on a set of high-accuracy observations of these targets.

#### **Point picking**

In the case that the aforementioned targets cannot be placed in all scans, different methods must be used to register different laser scan acquisitions. One of the different methods to perform registration without targets is through point picking. In this method, unique and distinguishable geometries in the scanned environment can be used to make an estimation of the rigid body transformation parameters for different scans. By selecting at least three different points in each scan that resemble the same real-world location, these transformation parameters can be estimated using least squares estimation in a fashion similar to the target-based method.

#### **Iterative closest point**

Another method of registration is the so-called iterative closest point method (Besl et al., 1992). This method involves the minimization of an objective function based on two different point clouds. The function to be minimized is the sum of the Euclidian distance between each point in a reference point cloud to the nearest point in the to-be-transformed point cloud. This method does require some initial alignment of the two different point clouds due to the minimization, which could converge to an inadequate solution.

## 2.3. Principal component analysis

Principal component analysis (PCA) is a statistical method that is widely applied in a large variety of disciplines such as geography, climatology, and psychology (Demšar et al., 2013). The original purpose of PCA is to reduce the dimensionality of a high-dimensional data set while maintaining a low error representation of the original data. Through the reduction of dimensionality, data can be represented in a way that is more fitting to visualise and interpret. Furthermore, PCA can be used to explore relationships between variables in a data set (Demšar et al., 2013).

For a data set, the variance-covariance matrix is computed. Following, the corresponding set of eigenvectors and corresponding eigenvalues of this matrix is computed. The eigenvectors resulting from this computation can be seen as the axes of a new coordinate system describing the data set, the eigenvalues represented the variance that is explained per eigenvector. For each observation, a new set of coordinates in this new coordinate system is obtained. The magnitude of a coordinate in the direction of a certain dimension is influenced by the correspondence to the eigenvector representing that dimension. Different terms are used to describe the eigenvectors, and the new observation coordinates (Wilks, 2011). In this thesis, principal component (PC) loadings refer to the new axes obtained through PCA, and PC scores refer to the coordinates of observations expressed using the new axes. If a sampled distribution used for PCA originates from a multivariate distribution which contains a similar distribution in two orthogonal directions, then the PCA eigenvectors representing the direction of variance of these two axes, are subject to large sampling variations because there is no dominant direction of higher variance for these two axes in the true distribution. For instance: Consider the directions of highest variance of a realisation of a cigar shape distribution using three orthogonal axes. The direction of the first axis is straightforward. However, the direction of the two remaining axes is arbitrary due to the circular shape in the plane orthogonal to the high variance axis. The directions of the two remaining axes would be very dependent on the particular samples of the distribution. In PCA this effect can be identified if multiple PCs have eigenvalues (representing the variance in that PC direction) of similar magnitude (Wilks, 2011), and these PCs form a so-called effective degenerate multiplet.

By treating each cell in a multi-dimensional raster data set as an independent observation, PCA can also be used to provide insights into spatial and temporal variations in a spatial data set (Wilks, 2011). For example, in Chao and Liao (Chao et al., 2019), PCA is used to identify gravity anomaly signals coherent in space and time around earthquake events using raster time series. By visualising for each raster cell the loading of a PC, spatial relations are identified. PCs of a multi-year Topographical data set are used to identify forcing events and mechanisms driving topographical change of different beaches (Larson et al., 1999). In a point cloud context, PCA eigenvalues and eigenvectors are commonly used on a neighborhood of points to extract geometric features such as 'planarity' or 'surface variation' describing the relations between points in point cloud neighborhoods (Hackel et al., 2016).

## 2.4. Related work

The PLS system used in this research is installed to identify snow (re)distribution on the HEF glacier in the Ötztaler Alps in Austria, by Voordendag (Voordendag et al., 2021). A more in depth description of this specific laser scanning setup is provided in Chapter 3. Voordendag et al focus on glacial processes, whereas the scanning setup also allows the observation of paraglacial processes in the slopes adjacent to the HEF. In order to automate the process of point cloud registration, a method utilizing corresponding points in panoramic reflectance images is proposed by Kang in (Kang, 2008). In this research, an approach similar to that of structure from motion photogrammetry is used to obtain transformation parameters describing the geometric relations between different laser scans with overlapping coverage. It is found that this registration procedure results in a sub-centimeter registration error for the scans used by Kang et al. In this research, registration is only performed on short-range scans. In research by Kuschnerus (Kuschnerus et al., 2021b), different deformation processes on a beach in Kijkduijn are detected using a PLS setup. A time series-based clustering is performed in order to distinguish the different deformation processes. Clusters are based on the Euclidian distance between the elevation time series per cell. Using the same PLS setup as the previously mentioned work, a spatiotemporal segmentation of the beach is presented by Anders (Anders et al., 2020). In this research, segments correspond to a single process that is defined over a certain area and time interval. This differs from Kuschnerus (Kuschnerus et al., 2021b) where similarity is based on characteristics of a full time series, such that clusters are only defined in space and not time.

# 3

## Data description

In this chapter, an overview is provided on the data that is used for this thesis. First, the characteristics of the used laser scanner are presented, after which an overview of the total data set resulting from this instrument is presented. Last, the area of interest is described.

### 3.1. Instrument

#### Instrument specifications and settings

The laser scanner used to obtain 3D scans of the area of interest is the Riegl VZ-6000. This scanner is designed for the scanning of snow and ice at long ranges. Hence, this instrument has a large maximum observable range of 6 kilometers. Because of the energy required for long range observations, a laser eye safety class 3B is given to the instrument. The laser beam wavelength results in more favourable reflection characteristics for snow and ice compared to conventional LiDAR beam wavelengths. Other relevant specifications and settings of this instrument in the used scanning setup are provided in Table 3.1

Feature	Value
Manufacturer	Riegl
Model	VZ-6000
Laser beam wavelength	1064 nm
Laser beam divergence	0.12 mrad
Maximum measurement range	6000 m
Pulse repetition rate*	30 kHz
Angular step width*	0.01°
Horizontal field of view*	157°
Vertical field of view*	60°
Scanning time*	≈ 45 minutes

**Table 3.1:** Instrument specifications and settings\*.

#### Instrument reference system

The reference system in which the scanner records its data is the so called "Scanner's Own Coordinate System" (SOCS). A visual representation of this coordinate system is shown in Figure 3.1. The coordinates of a measured location can be expressed in both cartesian coordinates X, Y and Z, as well as in spherical coordinates  $\phi$ ,  $\theta$  and range.  $\phi$  is defined as the rotation around the Z axis.  $\theta$  is the angle between the Z axis and the X/Y plane. Range is the Euclidian distance between the scanner origin and the reflection point. The X, Y and Z axis are defined relative to the stationary part of the scanner. Thus, while scanning, as the laser beam orientation changes, the  $\phi$  and  $\theta$  angles are altered throughout the scan. The instrument is located at 3250m elevation at  $46^{\circ}47'45N$   $10^{\circ}46'58E$ .

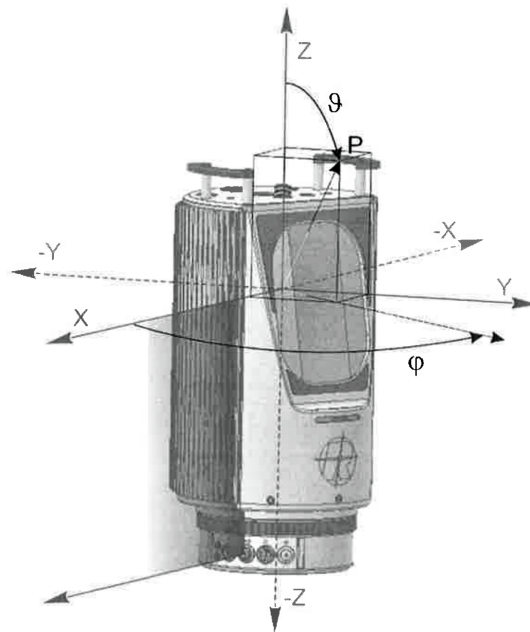


**Figure 3.1:** Scanner reference system as provided by its manufacturer Rieggl (Rieggl, 2014)

### Instrument setup

In order to allow a stable installation of the laser scanning instrument, the instrument is placed in a container, as shown in Figure 3.2. In this container, also a desktop computer is installed for the automation and data transfer of the scanner and webcams. Furthermore, a heating system is present to keep the indoor temperature stable and above the freezing point.



**Figure 3.2:** Container at the Im Hinteren Eis accommodating the scanning instrument and supporting facilities. This photograph is taken during a visit to the scanning system on 3 June 2022.

The container is placed on a metal beam structure which attaches the container to the surface. Within the container, the instrument is placed on a structure in a corner. A mechanical window is present in this corner, protecting the instrument when no observations are performed. When an observation is performed, the windows are opened and no material will be present between the instrument and the observed surroundings, as seen in Figure 3.3

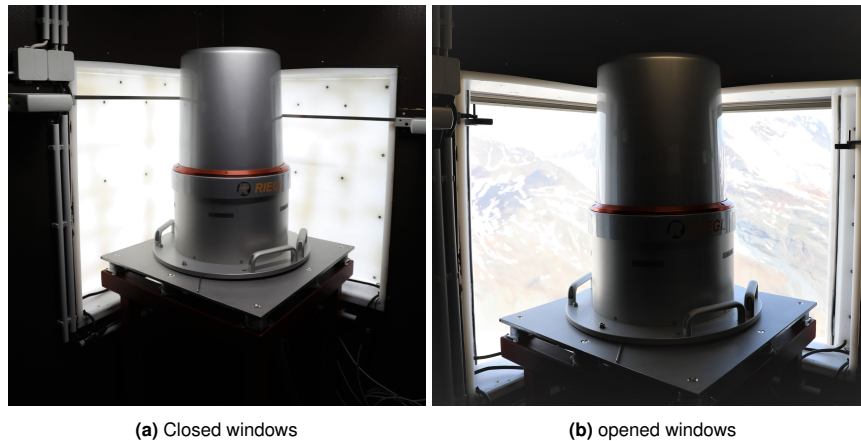


**Figure 3.3:** Demonstration of an opened and closed window of the scanner housing.

Besides the scanning instrument, in the container, also a computer is present. This computer is used to send the scanning data to an FTP server, after which the data is downloaded to a computer located at the Universität Innsbruck. This setup allows for the automation of the scanning procedure. A more in depth description of the automated scanning procedure is provided in Voordendag et al., 2021. Fully automated scans have been performed since June 2020 Voordendag et al., 2021. Since the start of the scanning in 2016, more than 800 scans have been made using the system.

In principle, every day a scan is performed by the PLS system. However, for this thesis, not all scans can be used. The analysed objects are the rock slopes at the counter slope of the PLS system. Therefore scans where these objects are occluded due to clouds cannot be used. Scans in which the rock slopes are largely covered by snow also cannot be used because otherwise range changes due to the snow cover would occur in the data set. Seldomly, the scanning system does not function properly due to problems with power supply, resulting in a few days without performed scans. an overview of the amount of usable scans per year is provided in Figure 3.4. The date at which the snow cover is deemed small enough to use the scanner observations, occurred four weeks earlier in 2022 compared to the other years, resulting in more usable scans during this period in 2022.

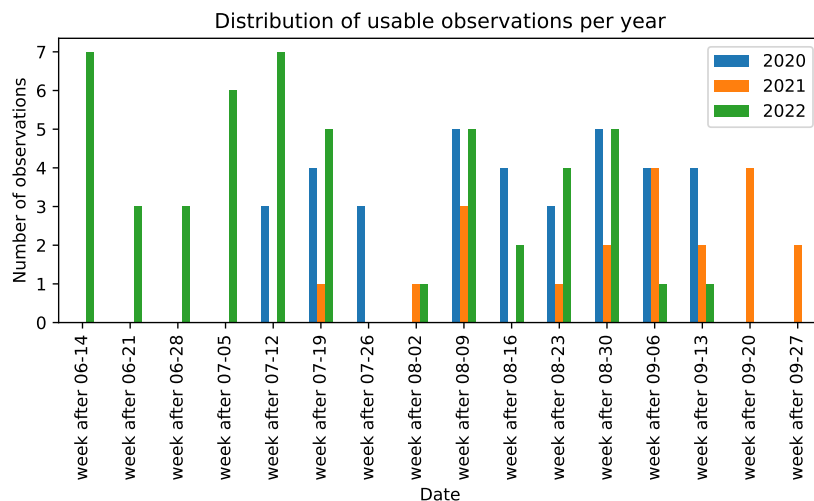


**Figure 3.4:** Usable scans per week for the years 2020, 2021, 2022.

### Data types

Resulting from an observation, per reflection point, the position of the reflection point is recorded, based on the viewing geometry and time of flight of the laser beam. Furthermore, the signal strength of the reflected laser beam is recorded, providing information on the reflecting material. In the used scanning

setup, to compute the reflectivity of a reflection point, the signal strength is corrected with the range observation to more consistently represent surface reflective properties. No correction is performed for the incidence angle per reflection point, resulting in similar objects having a different reflectivity in varying viewing geometry. Reflection can for instance be used for the identification of snow from rock (Prantl et al., 2017).

## 3.2. Errors and uncertainties

When analysing measurements, it is important to have an overview on the different processes which influence the measurements. A laser scanning range observation involves a laser source, transmitting medium, and a reflecting target. The laser source is the LiDAR instrument, The transmitting medium is the atmosphere, and the reflecting target is the object of interest. The source, medium, and target all introduce different types of uncertainties and errors in the range observation of the system. In the following subsections, the involved errors and uncertainties are discussed.

### Scanner stability

Due to instrumental limitations, the laser scanner is subject to vibrations which influence the laser beam orientation. The disturbance of this orientation can be estimated through internal inclination sensors. However, the measurement frequency of the inclination sensor in the instrument is low compared to the pulse repetition rate. This obstructs the correction for misorientations of individual scan lines caused by vibrations, as discussed by Voordendag (Voordendag et al., 2022). The magnitude of the errors caused by these high frequency vibrations are estimated to be in the decimeter scale in the vertical direction (Voordendag et al., 2022). In the closer range case of the Kijkdijjn PLS, these errors are estimated to be in the centimeter range (Kuschnerus et al., 2021b).

Besides self induced vibrations of the laser scanner, the instrument is also subject to changes in position and orientation caused by external factors. Although the sources of these disturbances are not exactly known. In the beach observation PLS setup described in Section 2.4, the weather is found to significantly influence the data quality of the multi temporal laser scans (Kuschnerus et al., 2021a). Furthermore, from the data collected by the internal inclination sensors of the scanner, it can be concluded that the scanner is not stable between different scans (Voordendag et al., 2022) Although the changes in position and orientation are small, they affect observations at long ranges.

### Atmospheric conditions

When light travels from one medium to another, refraction occurs, causing light beams to deflect corresponding to the reflective indices of the media it travels through. In air, the refractive index is dependent on the air temperature and (water vapour) pressure (Birch et al., 1993). Therefore, when a LiDAR beam travels through air containing a variation in temperature or (water vapour) pressure, the beam will be slightly deflected and reflect from a different location than in the case of atmospheric conditions constant in space. Furthermore, the velocity of the laser beam also depends on conditions of the air, causing variation of return signal time depending on air conditions. As it is not possible to measure the air temperature in the volume between the instrument and area of interest, the magnitude and direction of this deflection is unknown. Resulting, a different range will be observed than in the case of constant air temperature. The atmosphere is more stable in the early morning before sunrise. Thus, to mitigate the effects of temperature variations, observations are only performed between 2:00 and 4:00 in the morning, such that less variation in air temperature is present compared to during the day.

### Scanning geometry

The geometry in which observations are performed also influences the quality of the measurements. The laser beam emitted by the laser scanner does not represent a line, but rather a cone, such that when projected on a surface at a certain distance, the radiation of the laser will be distributed over an area instead of being focused on an infinitesimal area. The size of this area projected, the laser footprint, will increase with increasing laser beam divergence, distance to the laser scanner, and incidence angle of the reflecting area to the scanner (Soudarissanane et al., 2011). Due to the topography of the area of interest, a large variety of laser footprints occurs. A larger laser footprint introduces uncertainty in the location of reflection of the laser beam as this might occur anywhere in the laser footprint. In the area of interest, the major axis of laser footprints ranges from 0.2m at favourable distance and incidence angle,

to 3 meters in unfavourable viewing geometry.

### 3.3. Area of interest

In this research the identification of geomorphological processes will be performed on the rock slopes adjacent to the HEF, opposite of the IHE scanner. The elevation in this area ranges from around 2600 m at the glacier tongue to around 3400 m at the mountain ridges. The laser scanning instrument is located at an altitude of 3250 m (Voordendag et al., 2021).



**Figure 3.5:** Photograph of a large fraction of the area of interest, captured on 03-06-2022.

The total area captured by the laser scanner is shown in Figure 3.7, a large portion of this area is captured in the photograph of Figure 3.5. As can be seen in the photo, the area of interest is a peri- and pro- glacial region. Contained by the rock slope are three corrie glaciers, *Kesselwandferner*, *Langtaufererjochferner* and *Vernaglwandferner*. In various areas of the rock slope, the bedrock is covered by unconsolidated materials including at the boundary between the HEF and the rock slope, which is characterised by lateral moraines. A photograph of such a boundary location is shown in Figure 3.6, where unconsolidated material of a large variety of sizes can be identified. Last, various water streams and gullies can be found. In a previous study, around the area, numerous geomorphological processes have been identified, including: dead ice body melting, fluvial erosion and deposition, permafrost ice melting and rockfall events (Sailer et al., 2014).



**Figure 3.6:** Water streams and unconsolidated material at the boundary between the Hintereisferner and the rock slope on 03-06-2022.

Due to varying reasons, it is not possible to perform an analysis for the total field of view of the laser scanning instrument. In Figure 3.7 the red colored areas are part of the same slope as the scanning instrument, due to unfavourable geometry, the quality of the observations of these areas is insufficient. As this thesis does not focus on glacier change, also the glaciated areas indicated in blue are not part of the analysis. Green areas represent the mountain ridges which are used for the registration of range images as described in Section 4.3.3, and the purple area is used for the comparison of different registration methods, of which the results are presented in Section 5.1. Last, as the area undergoing the largest amount of topographical change in the data set, the yellow area is chosen as the area in which geomorphological processes are identified using PCA, with results presented in Section 5.2.3.

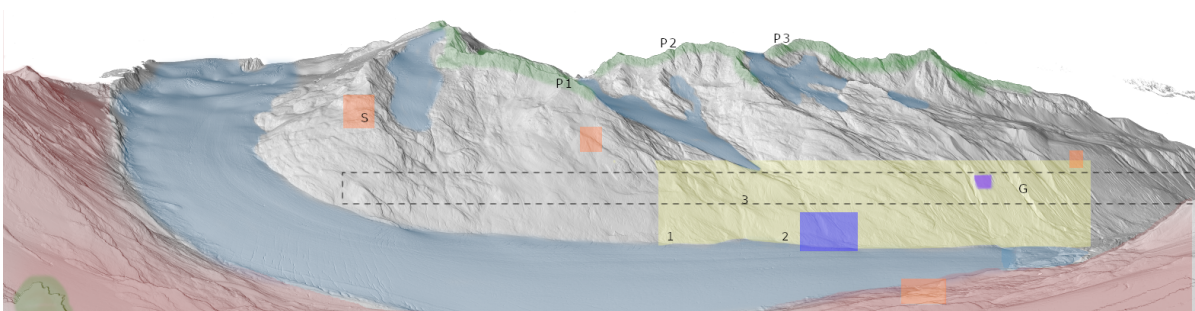


**Figure 3.7:** Relief shaded range image of the total scanner field of view. Colors indicate regions which are used for different purposes in this research. Blue zones indicate glaciers; The red zone indicates the slope on which the scanner is placed; The green zones represent the features used for image registration, discussed in Section 4.2.2; the orange zones represent the other zones considered for registration, also discussed in Section 4.2.2; the yellow zone refers to the area investigated using principle component analysis as discussed in Section 4.5; the purple zone refers to the area used for comparison of different range image and point cloud registration methods as discussed in Section 4.2.2; the dark blue zone represents the area depicted in Figure 3.6. The numbers 1, 2, and 3, refer to the example regions presented in Section 4.3.4 of steady change, sudden change, and little change, respectively. The G and S refer to the regions used to assess misalignment as discussed in Section 4.2.2. The dashed rectangle indicates the region over which the mean range difference is computed in the mountain ridge and stable region comparison presented in Section 5.1.

# 4

## Methodology

### 4.1. Workflow overview

In this section, an overview is provided on the different steps which are performed to create an automated range image registration procedure, create a 4D spatiotemporal dataset, and identify geomorphological processes in such a dataset. A flow diagram representing the workflow is presented in Figure 4.1:

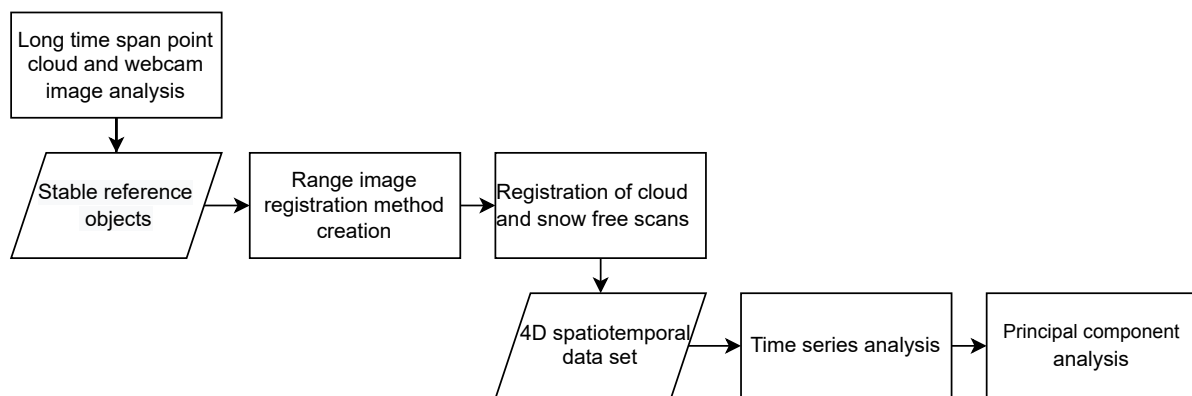


**Figure 4.1:** Flow chart representing the methodology of identifying geomorphological processes from the Im Hinteren Eis PLS data.

To facilitate the registration of laser scans, as discussed in Section 2.2.2, it is important to identify distinguishable stable objects which can be used as a reference in different scans. The procedure for the identification of this stable object is presented in Section 4.2, where the stable objects are identified through an iterative registration of two point clouds. Next, a method for the automated registration of the laser scans is developed, using the stable objects as a reference. This automated registration method is presented in Section 4.3. Using the automated registration procedure, for the summers of 2020, 2021, and 2022, all cloudless scans are converted to range images and registered to a single reference frame per year. After this registration, per year a 4D spatiotemporal dataset of these range images is created, allowing a time series analysis of range image changes. Finally, in order to obtain insights into the geomorphological processes, PCA of the 4D spatiotemporal data set is performed, which is described in Section 4.5.

### 4.2. Stable area identification

For the registration of different PLS observations, it is important to find regions in the scanned area which are not subject to surface elevation change. It is assumed that stable areas correspond to areas with little surface elevation change in the PLS data. To identify areas of little surface elevation changes at different time scales and different magnitudes, an analysis is made for different time intervals. At first,

surface elevation changes are determined through the difference between the first and last available observations in which no snow cover is present. Two point clouds are registered as discussed in Section 4.2.1.

### 4.2.1. Point cloud registration

No targets are placed in the view of the TLS instrument due to the technical challenges of establishing a construction that guarantees sufficient target stability in an environment subject to snowfall and heavy winds. Therefore, a registration is performed based on the measurements. In order to register these point clouds, which contain measurements of areas subject to large elevation changes between the observations, the following iterative method is performed:

The initial metric used to assess alignment is the cloud-to-cloud distance. This per-point metric is based on the Euclidian distance to the nearest neighbor point in a reference point cloud. To initiate the alignment, point picking is used, utilizing four points at locations in the point clouds which are likely to be relatively stable over the observation period: A ridge, the meteorological station, and two (sub)summits (indicated with P1, s, P2 and P3 in Figure 3.7 respectively). After this step, the following iterative sequence is started:

1. After the previous alignment is completed, the cloud-to-cloud distance is computed with the first scan as a reference.
2. All points in a homogeneous area with a large cloud-to-cloud distance are removed. These areas are assumed to be snow fields, glaciers, or subject to large magnitudes of erosion or deposition.
3. Using the ICP algorithm, the two point clouds are again aligned.

This procedure is repeated until the spatial distribution of the cloud-to-cloud distance stabilizes at a magnitude in the decimeter scale. This is not a signal of topographical change, but rather an artifact of the cloud-to-cloud distance metric. As the point sampling of the two different point clouds is not perfectly aligned, at a location, the cloud-to-cloud distance can be largely influenced by the fact that the reflections of the different scans do not sample the surface at consistent locations. Thus, without any topographical change, this could cause a cloud-to-cloud distance to become as large as half the point spacing of the individual clouds, which depending on the distance from the scanning instrument can be of multiple decimeters. An illustration of this problem is provided in Figure 4.2:

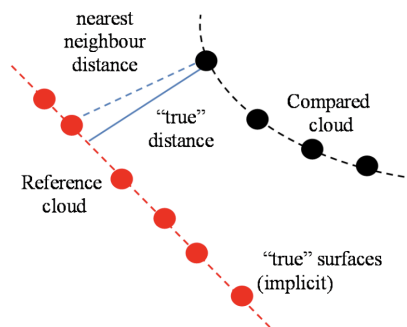


**Figure 4.2:** Visualisation of the nearest neighbor metric used in the C2C algorithm. Image source: Shen et al., 2017

To reduce the influence of point spacing artifacts to the topographical change metric, a different metric is used. A mesh is extracted from one of the scans using Delaunay triangulation. After this step, the cloud-to-mesh (C2M) distance between this new mesh and the point cloud is calculated to reduce the effect of misaligned point spacing. While the point spacing difference error will be reduced by computing the distance between the aligned observations, the interpolation error of the created mesh is a new error source. This error however, is assumed to be smaller than the point spacing error.

### Areas of little to no surface elevation

The areas with little to no surface elevation change in this initial analysis are assumed to be stable over the period of observations in this research. Due to uncertainties in the observations, there are

no areas where the calculated surface elevation change is exactly 0. Thus, to reduce the possibility of misclassifying an area as stable, an inspection of the C2M distance is performed. To classify an area as stable, the following must hold:

- The calculated surface elevation change shall be less than the expected accuracy of the PLS system (lower decimeter range (Voordendag et al., 2021)).
- Little spatial patterns or trends shall exist for the calculated surface elevation changes. (visually inspected)

After the stable areas are identified, their spatial extent is stored to be used for the registration of observations in later analyses. The areas found to be stable through this analysis are the two left orange surfaces in Figure 3.7.

#### 4.2.2. reference zones for registration procedure

To find the stable areas best used for the registration of range images as discussed in Section 4.3.3, numerous methods were performed. First, a point cloud registration was performed utilizing the techniques of point picking and ICP in the way described in Section 4.2.1. After this registration was performed, zones of little surface elevation change in the period between the two laser scan acquisitions were assumed to be stable. Alternatively, through webcam acquisitions, a different set of stable areas were also identified, by analysing colour changes over the course of the webcam image acquisitions. Lastly, it is assumed that the mountain ridges are stable. These areas are assumed to have been free of glaciation for centuries. Thus the surface is less influenced by paraglacial processes of significant magnitude because this effect is most prominent in the decades directly following deglaciation (Heckmann et al., 2019)

After the identification of different stable zones, the final choice of the zones used for registration was made by comparing the image registration based on key points originating from different stable zones. To gain an insight into the influence of surface elevation change on the zones considered stable, as well as the registration error occurring for two very similar acquisitions (small repetition time) the comparison is made for three different time intervals: 5 days, approximately 2 months, and 1 year. It is decided that the stable zones determined through the webcam images, and the point cloud analysis are used together because these individual collections of stable zones were not well distributed over the total range image. For both collections of stable zones, one zone is located on the same slope as the scanner to allow a better distribution of reference zones in the vertical viewing angle direction. For these two zones, the local topography results in a better incidence angle than other regions on the slope. The stability of these zones was assessed through webcam imagery. After the registration errors for the different combinations of scans and reference zones were calculated, the performance of the registrations was compared based on the following metrics:

First, a plot is made of the difference in range observations of each image pair. This plot provides the negative and positive range difference per pixel between the two images which should be properly aligned after registration. Especially in the case of the 5 days image pair, very little actual surface elevation change is expected. Therefore, the range differences between the image pair are likely a product of registration errors, as well as measurement errors. Registration misalignment can be assessed by looking at locations with large range differences between adjacent pixels resulting from the viewing geometry. In the case of a perfect registration, no large range difference should be visible between the two acquisitions. However, due to slight misalignment, it can be the case that in a performed registration, a pixel in one image actually corresponds to an adjacent pixel in the other image. At locations where in a single range image a large range difference occurs between adjacent pixels, this will result in a large range difference for pixels near these locations in a registered image pair due to the imperfect registration. By assessing this artifact in different locations, an assessment can be made of how well the images are aligned after registration. Two locations that fulfill this criterium are the Hintereis station, as well as the gullies present in the most northern zones in the region of interest.

The Hintereis station is a suitable location because viewed from the laser scanner location, the house sticks out of the rock landscape, thus creating a large range difference between pixels located on the house and pixels adjacent to the house. The gullies in the northern part of the region of interest are also suitable locations. Due to the low incidence viewing angle, adjacent pixels can have a large range

difference as shown in Figure 4.3. Furthermore, the gullies are located in an area where a lot of surface elevation change is occurring so the registration error in this area must be thoroughly assessed because the registration error is not constant over the total range of images.

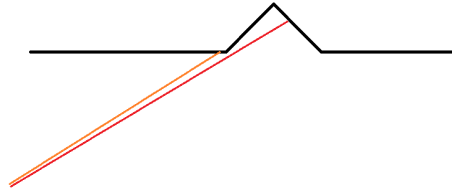


**Figure 4.3:** Representation of large range differences between adjacent pixels at gully edges resulting from the viewing geometry. The red and orange lines represent two adjacent viewing angles.

Next to visual inspection, also the mean difference of range in the area of interest is computed over the area marked with a dashed rectangle in Figure 3.7. Assuming that areas without topographical change in the used time intervals outnumber the locations undergoing change, the computed difference of range in the area of interest can serve as an indicator of registration quality. Better registrations are assumed to result in a lower total range difference in the area of interest. The results of this analysis are provided in Section 5.1.

#### **Comparison between the point cloud and range image registration**

To assess the errors resulting from the automated range image registration procedure, a comparison is made to a conventional point cloud registration method. This comparison is done for a region in the area of interest assumed to be stable based on webcam images. Therefore, any range difference between a scan pair should be the result of registration errors, alongside the errors and uncertainties as mentioned in Chapter 3. By converting a 1-hour separated and 1.5-month separated range image pair to point clouds after registration, a comparison can be made between the range image registration and point cloud registration methods. By converting one of the point clouds to a mesh, the C2M distance can be used as a metric of similarity between the scan pairs after different registration methods. Three types of registration are performed. On the 1-hour scan pair, the Riscan pro Multi-station adjustment registration is performed using the total scanning data per observation. Next, for both the 1-hour and 1.5-month scan pairs, ICP (Besl et al., 1992) is used to register a subset of the point cloud, which is represented as the purple zone in Figure 3.7. The results of this comparison are presented in Section 5.1.

### **4.3. Creating 4D spatiotemporal data set**

#### **4.3.1. Overview of steps**

In this section, the methods to create a 4D spatiotemporal data set from a series of PLS observations is presented. A flow diagram representing the workflow is presented in Figure 4.4.

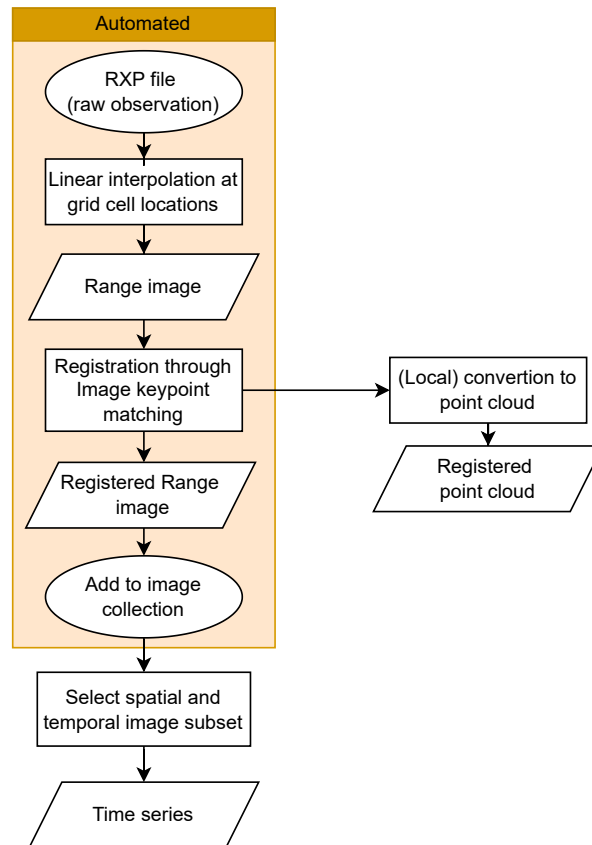


**Figure 4.4:** Flow diagram showing the process of creating an image collection time series from raw observations.

As a first step, a range image and reflection image are created from the raw observations. To be able to compare range and reflection images created from different observations, each pixel in the different images should represent the same viewing direction from the scanner location.

Due to different disturbances as discussed in Section 3.2, the scanner is sometimes slightly rotated between different acquisitions. A result of this disturbance is that the pixel locations of different range and reflection images do not always represent the same looking direction. Therefore, a registration procedure is needed to translate and rotate range and reflection images such, that the pixel coordinates correspond to a constant looking direction along the collection of images. This registration procedure is performed for each range and reflection image and will transform the images such that they correspond to a reference image. Before the registration can be performed, stable areas are identified, which can be used as a reference in the registration procedure of the range images. This identification of stable areas is discussed in Section 4.2.

When a collection of images is registered to the same reference image, the range and reflection changes along the different epochs within the image collection can be compared under the assumption that a pixel coordinate corresponds to the same looking direction in each range or reflection image. For each pixel location, a time series of the range and reflection can be created using all the observations in the image collection. The result is a time series data set of 3D observations, which is also referred to as a 4D spatiotemporal data set.

### 4.3.2. Conversion to range images

In order to properly convert raw laser scan observations to range and reflectivity images, first, different types of operations must be performed on the .RXP files. In this section, these different operations are presented. The raw format in which the range observations are provided by the PLS instrument is the .RXP format, which can be opened using Riegl licensed software such as RiScan pro or the RIVLIB libraries. This data format allows one to obtain point clouds with additional information per range observation, such as the intensity of the return signal. When obtaining the laser scanning data in the raw (.rxp) format, a custom script is used to convert the raw scanning data to an ASCII .txt file

containing a point cloud represented in spherical coordinates. So per reflection point, the observed range, horizontal viewing angle  $\phi$ , vertical viewing angle  $\theta$  (as defined in Section 3.1), and calculated reflectivity are stored. This spherical coordinate system is useful for creating range images because in an image, each pixel coordinate corresponds to a different viewing direction from an instrument origin, allowing conversion from the scanning observations to a range image or reflectance image format.

### Scanning pattern

In a range image, observed ranges are presented in a two-dimensional raster with orthogonal axes. The raster cell coordinates will relate to the spherical coordinates of the viewing direction for the corresponding range observation. The scanning pattern of the used instrument represents a sawtooth pattern as shown in Figure 4.5. This pattern does not allow a trivial conversion of range observations to a representation in a raster with orthogonal axes. Therefore a method of resampling is needed such that a proper representation of the data in a grid is possible.

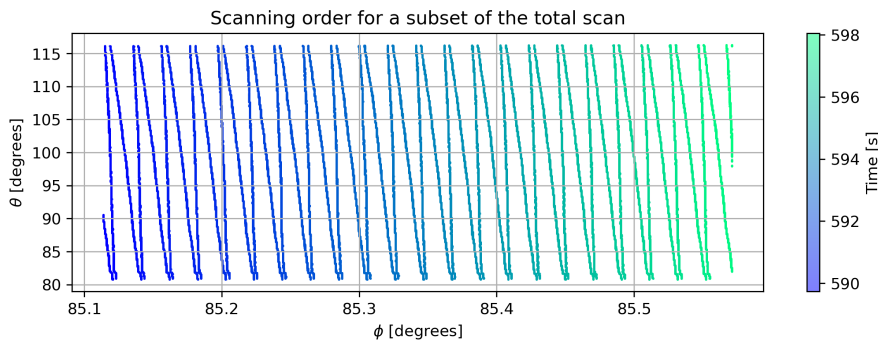


Figure 4.5: Scanning pattern of the laser scanning instrument in spherical coordinates.

### Discretisation

First, a discretisation approach is considered. In this approach, a  $\phi$  and  $\theta$  raster is created, and for each raster cell, the maximum range observation within this raster cell is chosen to represent the range in that raster cell. The cell size is chosen to correspond to the angular step size of the scanning system as presented in Section 3.1 such that most cells contain only a single observation and downsampling is limited. However, due to the sawtooth scanning pattern of the instrument, a repeating artifact arises where columns in the raster do not have a corresponding range observation whereas other columns have more than one observation, as shown in Figure 4.6.

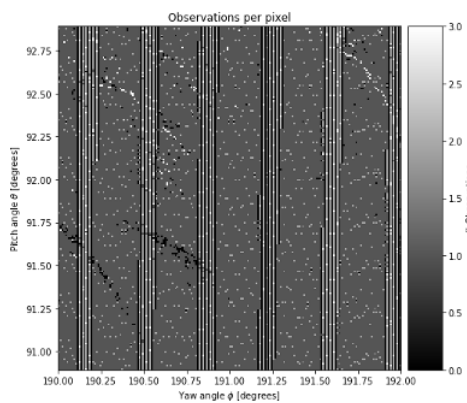


Figure 4.6: Number of original reflection observations per grid cell using the discretisation approach

### Interpolation

A more fitting approach to creating range images, utilizing a  $\phi$  and  $\theta$  raster, is through a linear interpolation of the entire data set. The interpolation is performed by Delaunay triangulation of the original

observations in spherical coordinates, after which a barycentric interpolation is performed at the grid locations (Virtanen et al., 2020).

Because the interpolation is based on Delaunay triangulation and barycentric interpolation, range and reflection values will also be computed for raster cells where no observation was originally present. Therefore, range interpolations will be made for looking directions containing no nearby observations, such as between mountain summits. This is undesirable, thus to mitigate these effects, a masking of the interpolation images is performed. The used mask is created by evaluating which pixels contain an actual observation. Next, to remove the unwanted scan line data gaps as shown in Figure 4.6 from the mask, a linear interpolation in the horizontal direction is performed for data gaps with a maximum length of two pixels. This way, all locations containing vertical data gaps due to the scanning pattern are not masked out of the interpolated image. Resulting, is a mask that masks out all pixels which for which no observation is present within a two-pixel distance.

The interpolation approach has two main advantages over the discretisation approach:

Firstly, the interpolation approach assigns a range or reflection value to each grid cell. Thus, no data gaps form, and this prevents the need for filling data gaps afterward. Secondly, More information of the original observations remains after the creation of a range images. In the initial approach, for each cell containing multiple range observations, only a single range observation would end up in the range image. Contrarily, in the interpolation approach, information of the three closest range observations is used for the interpolation at the grid cell locations.

Disadvantages of the interpolation approach compared to the discretisation approach are:

None of the range image cells correspond exactly to an actual original observation and are thus subject to interpolation errors. On the other hand, one could argue that a similar situation holds due to the discretisation in the initial approach. In that case, the original spherical coordinates of observations are altered to correspond to grid cell locations. Another disadvantage of the interpolation is the computational time, which is significantly longer compared to the initial method.

For the creation of range and reflection images in this thesis, the approach of interpolation is chosen for the creation of range images, as the advantages of this method outweigh that of the discretisation method. The interpolated grid, which will result in the range image is a grid with  $0.01^\circ$  step size in both  $\theta$  and  $\phi$ . This step size is chosen such that the amount of interpolated points roughly corresponds to the number of observations throughout the total grid. Thus, the original data is not significantly downsampled, and interpolation artifacts are of small enough influence. Furthermore, using this step size, projected on the surface of the area of interest, the pixel size will rarely exceed 1 meter, which is the maximum cell size to analyze fluvial and rockfall processes in high alpine terrain using airborne laser scanning (Sailer et al., 2014).

### 4.3.3. Range Image registration

Due to the large amounts of scans available through PLS, an automated scan registration procedure is beneficial and reduces the time involved with scan registration. A registration method is presented in which the registration is performed on the range images, exploiting areas subject to little surface elevation change and the nearly fixed scanner position.

To research the use of range images for analysis of the PLS data, it is fitting to perform the registration of the laser scan data using this data format as well. In a PLS setup, performing the registration of the laser scans using range images instead of point cloud data has multiple advantages. In this section, a method is presented which performs a registration based on range images instead of point clouds as is the case with the aforementioned methods.

In this section, the registration method for the range images is presented.

#### Input Data

In order to perform registration of the different laser scans, it is important to choose a feature to be used to estimate the transformation needed for proper image registration. Several usable parameters could be obtained from the laser scan data and expressed in a range image format:

- Reflectivity
- Range
- A shaded relief plot of the observed range

Each of these different features was considered to be used for the registration of the range and intensity images. Each of the different features has unique traits which could be exploited for the registration. In this section, a qualitative assessment of the performance of each data source as an input for the SIFT interest point extraction algorithm is discussed.

### Reflectivity

A feature that can be well interpreted is reflectivity. This parameter is obtained through some corrections of the observed return signal intensity as discussed in Figure 3.1. When viewing a reflectance image, this is most similar to an optical observation, such as a panchromatic image, and has been successfully used for the registration of LiDAR data in combination with optical data and the SIFT algorithm (Abedinia et al., 2008). An example reflectivity image is presented in Figure 4.7. A key difference between camera observations and LiDAR reflectance observations is the type of observations, which are, respectively, passive and active. Therefore, LiDAR reflectance images are (during the night) not influenced by the illumination of the observed region. This could cause some decline in the performance of the SIFT algorithm as the passive observation type will have fewer artifacts such as shadows, which might result in qualitative key points.

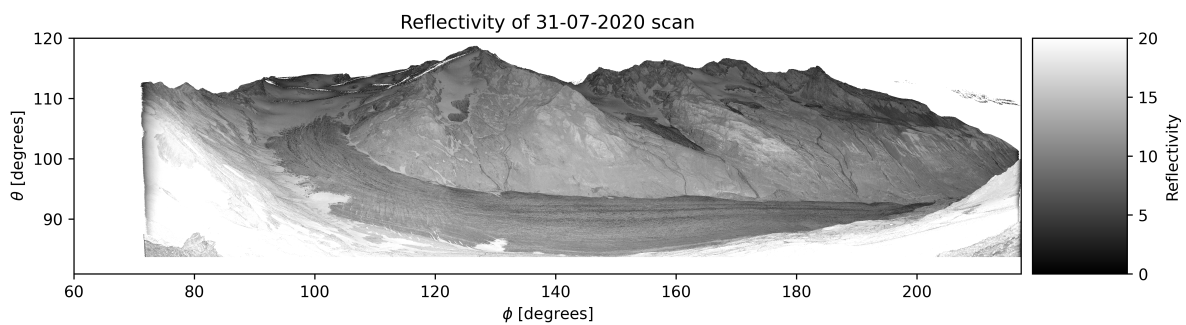


**Figure 4.7:** Reflectivity image of the laser scan on 31 July 2020, as considered for the generation of key points.

### Range

Range observations are dependent on the distance to the reflecting medium. Because of the observation geometry of the laser scans, the range observation over the total area of interest span approximately from 6 to 4500 meters. Because of this large range of values, and little relief in the observation direction of the scanner, there are not a lot of regions with a proper variation of range at smaller spatial scales, as can be seen in Figure 4.8. For the feature extraction using SIFT, which finds points of interest through the difference between different blurring magnitudes, it is important to have significant contrast on low spatial scales. Therefore, this type of data is not very fitting for the usage in SIFT, as it will result in a small number of key points found with bad quality.

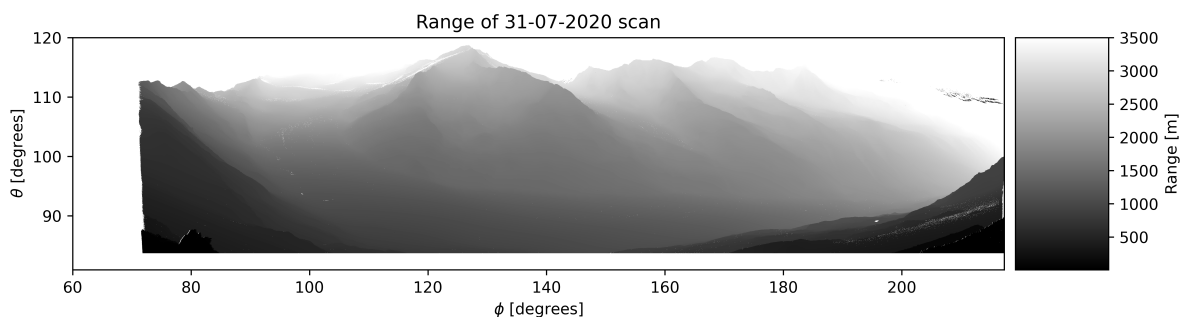


**Figure 4.8:** Range image of the laser scan on 31 July 2020, as considered for the generation of key points.

### Range shading

A different way to use the range observations as a data source for the registration of the range images

is through the creation of a hillshade of the range observations. Usually performed on DEMs, this transformation creates per pixel illumination based on the local surface elevation gradient. This gradient is estimated through a discrete 2-dimensional convolution with a window function in two different directions. The end product is a hillshade as seen in Figure 4.9 which is based on the local relief gradient of a pixel, as well as the desired illumination angle. An advantage of this hillshade technique compared to the normal range observations is the smaller span of the data. The hillshade illumination may span from -1 to 1 and is not dependent on the absolute range value per pixel, which creates a datatype with contrast that is homogeneous over the total area of interest, and contains enough variation at lower spatial scales, such that interest points can be obtained from the data. It is found that the usage of the range shading as input for the SIFT image feature detection algorithm results in the largest amount of key points, as well as the highest resemblance of the key point matches after image matching. Therefore, it is chosen to use this data as the input for the SIFT algorithm in the image alignment procedure.

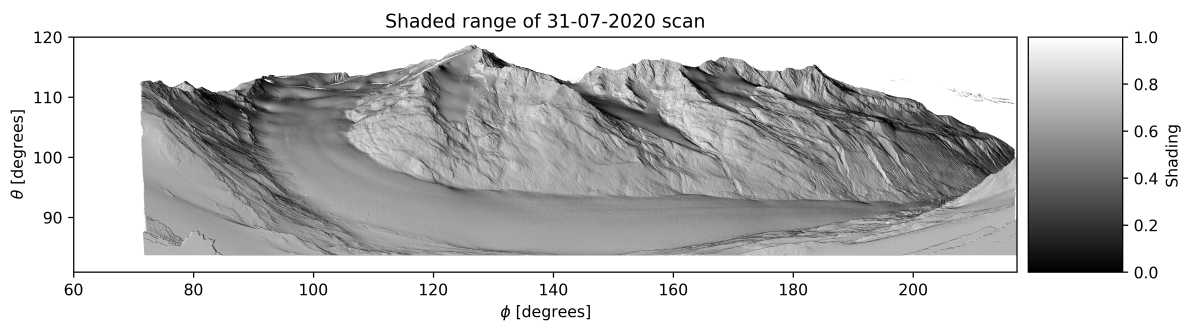


**Figure 4.9:** Shaded relief range image of the laser scan on 31 July 2020, as used for the generation of key points.

### Registration steps

The used registration procedure is a sequence of different steps. A flow diagram providing an overview of the different registration steps is provided in Figure 4.10.

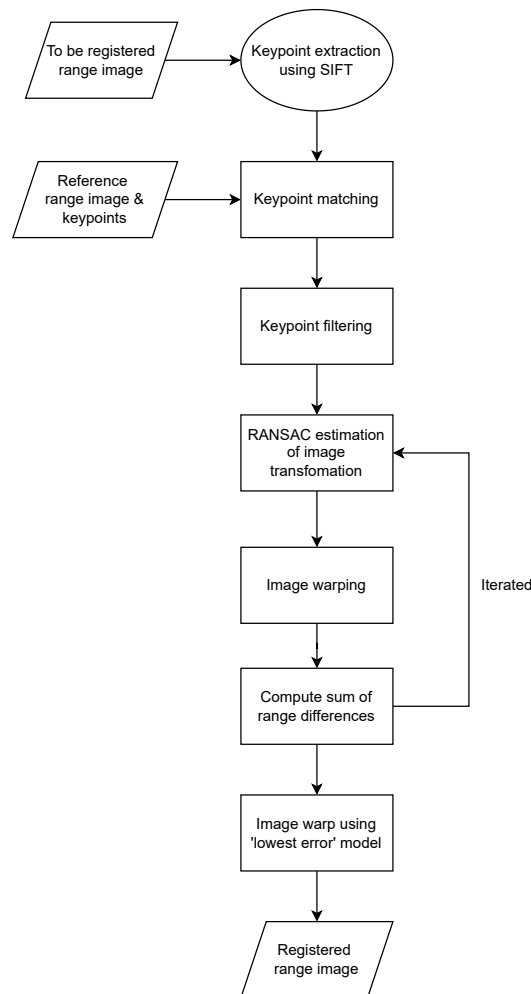


**Figure 4.10:** Flow diagram showing the process of registration of a range image to a reference range image coordinate system.

### Stable area masking

As discussed in Section 4.2.2, reference points must be located in stable areas to allow a consistent registration. After these stable areas are identified, they are selected in the reference image, and a mask is created through which only the areas considered stable are part of the input for the SIFT image feature detection. Since not every image is already roughly aligned, if masking would be applied to both the reference and analyzed image, the masks could be applied to different zones, which would result in different areas being masked out in the different images, resulting in no key point matches. Therefore, masking is only applied to the reference range image.

### SIFT image feature extraction and feature matching

As mentioned in Section 2.2, the most vital step of the registration procedure is the image feature extraction step. Through the use of the SIFT algorithm (Lowe, 1999), these features can be obtained. SIFT takes as input an image and alters this image in numerous ways in order to find these features. The found image features contain two properties: A key point, which is the feature location expressed in image coordinates, and a descriptor, which is a vector in which information about the surrounding pixels of the feature is stored.

The SIFT algorithm applies two different types of operations on the input image. First, the image will be downsampled to a set number of scales. Next, for each of these scaled versions, a Gaussian blurring is applied on a set range of magnitudes. The result is several copies of the input image, each subject to different magnitudes of downsampling and blurring. Following this step, the difference of Gaussian is calculated, which is the result of a subtraction of two images blurred on different scales. Locations in the image with local minima and maxima of the difference of Gaussian are then determined to be potential

features. In the next step, the features lying on an edge or in a low-contrast region are removed from the list of potential features. After a final list of key points is determined, the corresponding descriptors are computed. To compute a descriptor vector, a 16 by 16 grid around the key point location is used to compute 8 gradients in different directions for 16 locations within the grid. This combination of gradients is then expressed in a 128-size vector which is later normalized. Resulting from the SIFT algorithm is a list of key points with a corresponding list of descriptors that can be used to assess the similarity between two features on different images. An example of the key points resulting from SIFT when using a masked shaded relief image as input is provided in Figure 4.11a.

After a list of key points and descriptors is obtained for a pair of images, the key points corresponding to the same objects in the different images can be identified through feature matching. In this step, for each key point, the similarity of its descriptor is compared to all descriptors obtained from the other image. A match is created for the nearest neighbor found using the Euclidian distance between the descriptors. A pair is omitted if the second nearest neighbor distance is not larger than a certain threshold of the nearest neighbor distance.

Resulting from the feature matching step is a list of indices, providing which key points from the two different images are corresponding to the same location based on their respective descriptors. This list can then be used to estimate the image transformation required to align the two different images based on the image coordinates of the feature matches in the two different images.

### Key point filtering

After a list of matching key points is obtained, the resemblance of the key points is further assessed independent of the SIFT input data, by computing the mean absolute difference of the observed range values in the neighborhood of the key points. By filtering key points based on this metric, key point pairs with two different undesirable traits are removed from the key point matches list used for the alignment of the range images. First, key points that do not represent the same location are removed as there is a small chance that two different features would have a very high similarity of observed ranges in their neighborhood. Next, key points that are subject to surface elevation change between the two images are also removed, because an actual surface change would result in a relatively large difference of ranges in the neighborhood of the key point, and thus a large mean absolute difference of the observed range values around the key point.

The neighborhood mean absolute range difference for a key point pair  $[x_b \ y_b]^T$  and  $[x_a \ y_a]^T$  found for range images  $R^b$  and  $R^a$  is defined as follows:

$$\Delta R_{neighborhood}(R^b, R^a) = \sum_{j=-5}^5 \sum_{i=-5}^5 (R_{x_b+i, y_b+j}^b - R_{x_b+i, y_b+j}^a)^2 \quad (4.1)$$

In this equation,  $x_a$  represents the  $x$  coordinate of the key point of image a etc. Filtering to the different range images then can be applied by setting a threshold for the maximum allowed range image neighborhood mean absolute difference. An example of the reduction in the number of key points after filtering is provided in Figure 4.11

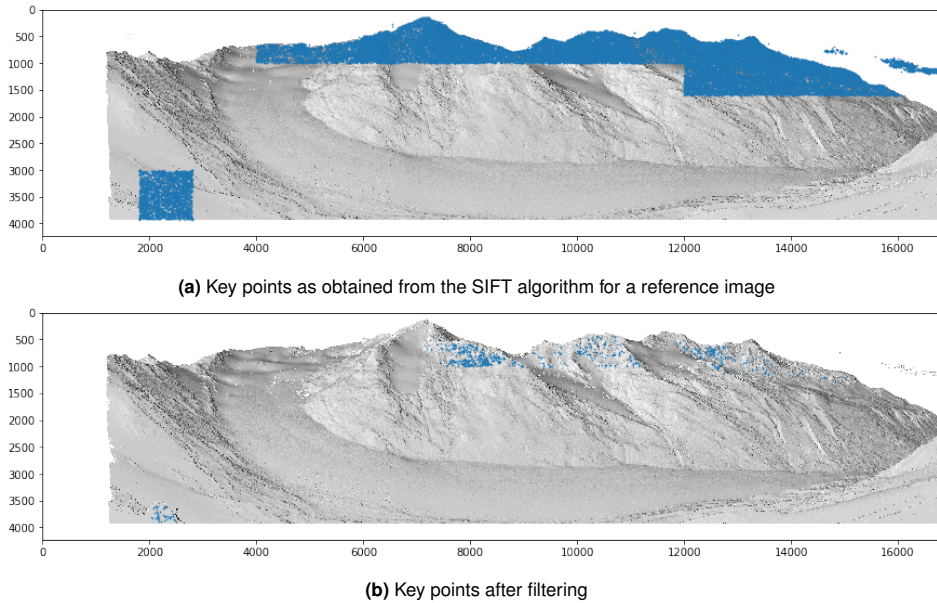


**Figure 4.11:** Demonstration of the reduction in number of used keypoints after keypoint filtering.

### Estimation of the image transformation

Once a list of reliable key point matches between two images is obtained, there is still a possibility of outliers being present, which would influence the estimation of the image transformation unfavourably. Therefore, it is chosen to use the random sample consensus (RANSAC) (Fischler et al., 1981) procedure to estimate the image transformation parameters based on the key points pairs. This algorithm is frequently used in the problem of key point matching, such as in structure from motion (Smith et al., 2016).

The RANSAC procedure can be used to increase tolerance to outliers in model parameter estimation problems. The algorithm starts with the selection of an initial random subset of an input data set. Using this subset, a specified model parameter estimation is performed. After the model is estimated, the residuals of each data point in the total data set are calculated. Following, the data set is split into outliers, which are data points where the residual exceeds a certain threshold, and inliers, where the data point residuals to the estimated model are within the set error threshold. The number of inliers is stored, after which a new random subset is selected, and the aforementioned sequence of steps is repeated. After a set number of iterations, the model estimate with the largest resulting amount of inliers is chosen to be the best corresponding model estimation to the data set.

In the case of the implementation of RANSAC for estimation of image transformation parameters based on the key point matches, the input data set is the list of corresponding key points between the two different images. The model to be estimated is the matrix transforming the homogeneous image coordinates of one image to the other image coordinate space as provided in Equation 4.2.

$$\begin{bmatrix} X \\ Y \\ 1 \end{bmatrix} = \begin{bmatrix} a & b & c \\ d & e & f \\ 0 & 0 & 1 \end{bmatrix} \begin{bmatrix} x \\ y \\ 1 \end{bmatrix} \quad (4.2)$$

As discussed in Section 3.2 and (Voordendag et al., 2022) between scans, the scanner is assumed to be able to rotate as well as change position slightly. Because the scanner movement is not expected to exceed a few centimeters, the influence of this movement is very small compared to the rotations of the scanner and the other uncertainties of the instrument. Therefore, for the registration of the range images, the assumption is made that no movement occurs between scans, allowing the use of key points originating from objects which do not lie on a single plane to be used for the registration of the images. The rotations of the scanner between scans results in rotations and translations of objects appearing in the range images due to the rotation of the scanner coordinate system. Thus the fitting transformation to transform coordinates from one image coordinate space to another is a Euclidian transform, for which

6 parameters must be estimated as shown in Equation 4.2. To estimate this transformation, a minimum of three key point pairs are required to fix a transformation. The model estimation is performed using unweighted least squares estimation. The computation method of the transformation matrix using least squares estimation by Umeyama (Umeyama, 1991) is used to compute the Euclidian transformation matrix based on the key point location vectors in the input image coordinate system (corresponding to the right vector in Equation 4.2), and the key point location vectors in the reference coordinate system after projection (corresponding to the left vector in Equation 4.2).

After the least squares estimation of the transformation parameters is performed, using the key point matches, the inliers and outliers can be determined according to the RANSAC algorithm. Choosing a different amount of redundancy for the model estimation, and a different error tolerance for inliers in the RANSAC algorithm could change the outcome of the model estimation using the RANSAC algorithm. Therefore it is chosen to perform the RANSAC algorithm with a range of redundancy in model estimation and inlier error tolerance. Each final RANSAC estimation is then assessed by warping one of the images into the reference image coordinate system according to the estimated transformation, after which the two range images are subtracted. This results in a difference of range image, where if no natural change would occur, and alignment would be perfect, a cell value should be zero. When misalignment occurs as a result of inadequate model estimation, a difference of range will be present and cell values will have a larger magnitude than zero at locations where no actual change occurs.

Under the assumption that the amount of cells where no actual physical change is expected is always significantly greater than the number of cells where change is expected in the region of interest, the RANSAC transformation estimation with the lowest resulting median absolute deviation of the difference of range image in the region of interest is assumed to be the best model estimation and is used for the registration of the input image to the reference image. When warping the input image using an estimated model of sufficient quality, the input image pixel coordinates system corresponds to that of the reference image, such that range observations per pixel can be assumed to represent the same reflection points, thus completing the registration of the input image.

#### 4.3.4. Time series creation

With the possibility to automatically create referenced range images from the PLS observations, large numbers of observations can be converted to range images, referenced, and stored in a single data set. This data set then contains the range image at different epochs. The format of storing 3D observations for multiple epochs is called a 4D spatiotemporal data set. To limit the size of such a data set, it is chosen to create one referenced 4D spatiotemporal data set per year (only using summer data as explained in Chapter 3). The dates of the used scans per data set are presented in Figure 3.4. To provide some insight into this data set, three example subsets of the 2022 spatiotemporal data set are presented in Section 5.2.1. One example (referred to as the sudden change example) shows an area undergoing both positive and negative change at two different locations. Another example (referred to as the steady change example) shows an area subject to a steady rate of change. Last, an example area (referred to as the little change example) with little changes is presented. The locations of these example areas are indicated in Figure 3.7 using the numbers 1, 2, and 3.

### 4.4. Low variation areas

Because masking is applied in the PCA method, a part of the AOI is not yet analyzed. Because the masked-out areas are of low variance, there can still be changes occurring at smaller scales than the changes found using PCA. In order to detect changes of small magnitudes, the data in the area of interest will be aggregated. By taking the mean of a cell neighborhood, the influence of random uncertainties decreases relative to the occurring change magnitude according to the central limit theorem. By also taking the mean of multiple scans per area, the influence of errors that are constant or spatially correlated per scan will also be lowered. For the years 2020 and 2022, mean range change is calculated for each cell by computing the 40 by 40 cell neighborhood mean range for each epoch. Next, the temporal mean of the resulting dataset is computed for the first 10 and last 10 epochs of the 4D spatiotemporal dataset. By subtracting these two mean ranges, the resulting mean range difference is based on both spatially and temporally aggregated observations.

## 4.5. Principal component analysis

Once a 4D spatiotemporal data set is created from a sequence of registered observations, a method is required to isolate and analyze different types of topographical changes within the data set. As mentioned in Section 2.4, different techniques such as clustering have been used to link locations subject to similar change patterns. In this section, a method utilizing PCA of the created 4D spatiotemporal data sets is presented.

### PCA steps

To create interpretable results from the PCA, using the 4D spatiotemporal data set, a procedure is created. The sequence of steps in this procedure is as follows:

1. Select a subset of the 4D spatiotemporal dataset to analyse
2. Filter out raster cells at undesired locations
3. Reshape the dataset to 2 axes by combining the spatial axes into one axis.
4. Subtract the mean of each time series.
5. Calculate PC loading and scores
6. Perform varimax rotation of PCs
7. Identify effectively degenerate multiplets using North's rule of thumb (North et al., 1982)
8. Combine principal components making up effectively degenerate multiplets
9. Interpretation of temporal and spatial relations in PCs

Steps 1 until 4 deal with the preparation of the chosen 4D spatiotemporal data to be used in the PCA. The fifth step involves the computation of the PCs. In the remaining steps, the computed PCs are interpreted and possibly altered to aid interpretation.

### Step 1 until 4: preparing the 4D spatiotemporal data for PCA

The PCA is based on the range changes in a chosen subset of the 4D spatiotemporal dataset. First, a subset is chosen, which in this thesis is the yellow area indicated in Figure 3.7, at all usable summer epochs of 2022. To compute the range change, the observed range of the first epoch is subtracted from the total subset. The objective of this analysis is to identify areas subject to paraglacial geomorphological change. Thus, the snow and ice surfaces and cells in the subset representing these surfaces are masked out. To limit the influence of errors on the computed PCs, areas with little range variation are also masked out in the dataset used for PCA. A criterion for cells to be included in the PCA is that the standard deviation of their corresponding range time series must be larger than 0.15 m. For cells with a standard deviation below this threshold, it is assumed that a large part of their signal results from errors. Initially, the data set spans 3 dimensions ( $\phi$  angle,  $\theta$  angle, and time) while the data must be represented in two dimensions for the PCA. Therefore the masked range images per date are reduced to a vector by combining the  $\phi$  and  $\theta$  axis into a single axis. Next, for each time series, the mean is subtracted such that the time series vector represents the anomalies of the range time series. The result is a matrix  $X$  where each row corresponds to a different epoch, and every column represents a different raster cell. The data in this matrix are the range differences to the first epoch. Due to the varying ground sampling distance of the PLS system in the observed area, close-by objects with small incidence angles are more represented in the dataset than further away objects with low incidence angles. Because the highly varying and changing topography complicates the creation of an accurate scaling model, and due to time constraints, in this thesis, no scaling is applied to compensate for the heterogeneous representation of real surface elevation changes on the range changes represented in the dataset and PCA.

### Step 5: computing principal components

In this step, the PC scores, loads, and eigenvalues are computed. PC loads are the eigenvectors of the covariance matrix of a data set. PC scores are the result of the projection of PC loadings onto the original data set. PCs are computed for the matrix  $X$ , which is prepared in the previously described steps. With  $m$  epochs and  $n$  raster cells used, the size of the data set is  $m \times n$ . The covariance matrix  $C$  of  $X$  is obtained through:

$$C = \frac{1}{m-1} X^T X \quad (4.3)$$

$C$  is of size  $n \times n$  with  $m$  eigenvectors in  $\mathbb{R}^n$ . However, because of the large number of raster cells  $n$ , it is better to first transpose  $X$  to obtain the same  $m$  eigenvalues of the variance-covariance matrix, in order to prevent the eigenvalue computation for a  $(n \times n)$  matrix. The  $m \times m$  covariance matrix of  $X^T$  is computed according to the following equation:

$$C^* = \frac{1}{m-1} X X^T \quad (4.4)$$

When the covariance matrix  $C^*$  ( $m \times m$ ) is computed, its eigenvalues  $\lambda$  are obtained using Equation 4.5 (Lay et al., 2015):

$$\det(C^* - \lambda I) = 0 \quad (4.5)$$

The  $m$  dimensional eigenvector  $e_k^*$  corresponding to eigenvalue  $\lambda_k$  is found by solving the following linear system (Lay et al., 2015):

$$(C - \lambda_k I) e_k^* = 0 \quad (4.6)$$

Lastly, using the fact that if  $v$  is an eigenvector of  $X X^T$ , then  $X^T v$  is an eigenvector of  $X^T X$ , the  $n$  dimensional eigenvector  $e_k$  of  $C$  corresponding to eigenvalue  $\lambda_k$  of  $C$  are found using the following equation:

$$e_k = \frac{X^T e_k^*}{\|X^T e_k^*\|} \quad (4.7)$$

Resulting from the previous computations is a set of  $m$  eigenvalues  $\lambda_k$  and eigenvectors  $e_k$  of the  $n \times n$  covariance matrix of dataset  $X$ . By projecting the eigenvectors on the original data matrix  $X$  at epoch  $i$ , the PC score  $y_k(i)$  for PC  $k$  at epoch  $i$  are obtained:

$$y_k(i) = X(i)^T \cdot e_k \quad (4.8)$$

The result of the above computations is an orthonormal set of PC loading vectors in  $\mathbb{R}^n$  with corresponding eigenvalues and PC score vectors in  $\mathbb{R}^m$ . The first PC loading vector represents the direction of largest variance in the data set  $X$ . By reshaping the PC loading to the original image shape (recreating the  $\phi$  and  $\theta$  axis), spatial patterns of this PC can be identified. The corresponding PC scores represent the change of correspondence of a certain epoch to the relations described in the PC loading.

### Example calculation of principal components

To illustrate the computation of PCs for a 4D spatiotemporal dataset, an example calculation is presented: In this example, the 4D spatiotemporal dataset contains range observations sampled at four different viewing directions, and sampled at three different epochs. By preparing the dataset such as described in steps 1 to 4, we obtain the following  $(3 \times 4)$  example matrix:

$$\begin{bmatrix} 0.5 & 0.4 & -0.45 & 0.05 \\ 0.55 & 0.47 & -0.42 & 0.03 \\ -1.05 & -0.87 & 0.87 & -0.08 \end{bmatrix}$$

Using Equation 4.4, the resulting  $(3 \times 3)$  variance covariance matrix of this matrix is:

$$\begin{bmatrix} 0.3075 & 0.32675 & -0.63425 \\ 0.32675 & 0.35035 & -0.6771 \\ -0.63425 & -0.6771 & 1.31135 \end{bmatrix}$$

The three eigenvalues of this matrix are  $\lambda_1 = 1.97$ ,  $\lambda_2 = 1.47 \cdot 10^{-3}$ ,  $\lambda_3 = -2 \cdot 10^{-16}$ , and the corresponding eigenvectors are:

$$e_1^* = \begin{bmatrix} -0.39 \\ -0.42 \\ 0.81 \end{bmatrix}, e_2^* = \begin{bmatrix} -0.71 \\ -0.70 \\ 0.01 \end{bmatrix}, e_3^* = \begin{bmatrix} 0.58 \\ 0.58 \\ 0.58 \end{bmatrix}$$

The presented vectors are the eigenvectors of the variance covariance matrix of the transposed example matrix. To obtain the (four-Dimensional) eigenvectors of the original example matrix, using the example matrix and the 3-dimensional eigenvectors in Equation 4.7, yields the following four-dimensional eigenvectors of the example matrix variance covariance matrix (the principal component loadings):

$$e_1 = \begin{bmatrix} -0.65 \\ -0.54 \\ 0.53 \\ -0.05 \end{bmatrix}, e_2 = \begin{bmatrix} 0.20 \\ 0.54 \\ 0.76 \\ -0.29 \end{bmatrix}, e_3 = \begin{bmatrix} 0.32 \\ 0.64 \\ 0.64 \\ -0.28 \end{bmatrix}$$

Finally, by projecting these vectors onto the original data matrix, the principal component scores are obtained:

$$y_1 = \begin{bmatrix} -0.78 \\ -0.84 \\ 1.62 \end{bmatrix}, y_2 = \begin{bmatrix} -0.04 \\ -0.04 \\ 0.00 \end{bmatrix}, y_3 = \begin{bmatrix} 0.11 \\ 0.20 \\ 0.31 \end{bmatrix}$$

### Step 6 to 9: interpretation of principal components

If no physical processes are identified through temporal and spatial patterns in the PCs, a varimax rotation (Kaiser, 1958) of the PC loading vectors is performed, which is a commonly applied technique when interpretability of the PCs is desired (Wilks, 2011). After rotation, effectively degenerate multiplets (as discussed in Section 2.3) are identified using North's rule of thumb (North et al., 1982) which estimates PC sampling error using the PC eigenvalues and the population size. If identified, the PCs in the degenerate multiplet are used to create a new PC through a linear combination of the PCs which creates a result suitable for interpretation. For the PCs with significant eigenvalues, the PC loading vector image and scores are visualised and used for the identification of geomorphological processes. Furthermore, a false colour image is created, where the red, green and blue intensity correspond to the loading of three (combined) PCs with differing score behaviour. since PC loading vectors are unit length, a vector with concentrated loading will have higher loading values. To combat this imbalance between the loading of different PCs for the false colour visualisation, not the loading, but the relative loading is used as a value for intensity. The relative loading at a raster cell for a PC is defined as the percentile of the raster cell loading in the total loading distribution of the PC. This way, an imbalance of different colours in the false colour image is mitigated. To compare the relations in the dataset found through PCA to the original data, the loading of the PCs is inspected at the three example regions described in Section 4.3.4.

# 5

## Results

In this chapter, the results from the above-explained methods are presented and described. First, results regarding the development and validation of the automated range image registration method are treated in Section 5.1. Following, results regarding the identification of geomorphological processes are presented in Section 5.2.

### 5.1. Range image registration

This section presents the results regarding range image registration. First, a comparison of different reference zones in the registration method is presented. Next, the range image registration method is evaluated by comparing registration results to an ICP-based registration in the purple area in Figure 3.7.

#### Registration reference areas

As described in Section 4.2.1, to find a more fitting set of reference objects for the range image registration method, a registration is performed using mountain ridges, as well as using stable areas identified after point cloud registration and using webcam images. The results of the range image registration using these different reference areas at different time intervals are presented in Figure 5.1:

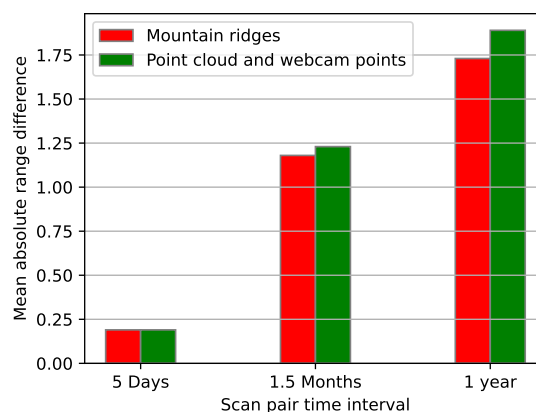


**Figure 5.1:** Combinations of time intervals and registration zones considered for the determination of the to-be-used fitting zone. the mean absolute range difference is computed over the area indicated in Figure 3.7

It can be seen that using the mountain ridges as a reference region for the registration of range images results in a slightly lower or equal total range difference between the registered range images at the three different time intervals. Therefore, it is assumed that mountain ridges are a better fitting reference area than the stable zones identified using point cloud registration and webcam images. Furthermore, using both reference regions, the 5-day scan pair registration results in a total error that is nearly three

times lower than in the other scan pairs. This could have multiple causes, which are discussed in Section 6.1.

### Before and after registration comparison

In order to gain insights into how the automated range image registration compares to the conventional ICP point cloud registration method, different comparisons are made. The area used for this comparison is indicated in purple in the overview image Figure 3.7. For this comparison, two different scan pairs are used, one pair with two scans that are just 1 hour apart (06-11-2020 02:00 and 03:00), and one pair where the scans were acquired 1.5 months apart (31-07-2020 and 15-09-2020).

Firstly, a comparison is made between the range differences of the two image pairs before, and after registration. The range differences are assumed to be residuals as no change is expected between the different scans. An overview of the spatial distribution of the residuals before and after registration is provided for the 1 hour and 1.5 months image pairs in Figure 5.3 and Figure 5.4 respectively. Histograms showing the distribution of the residuals are provided in Figure 5.2.

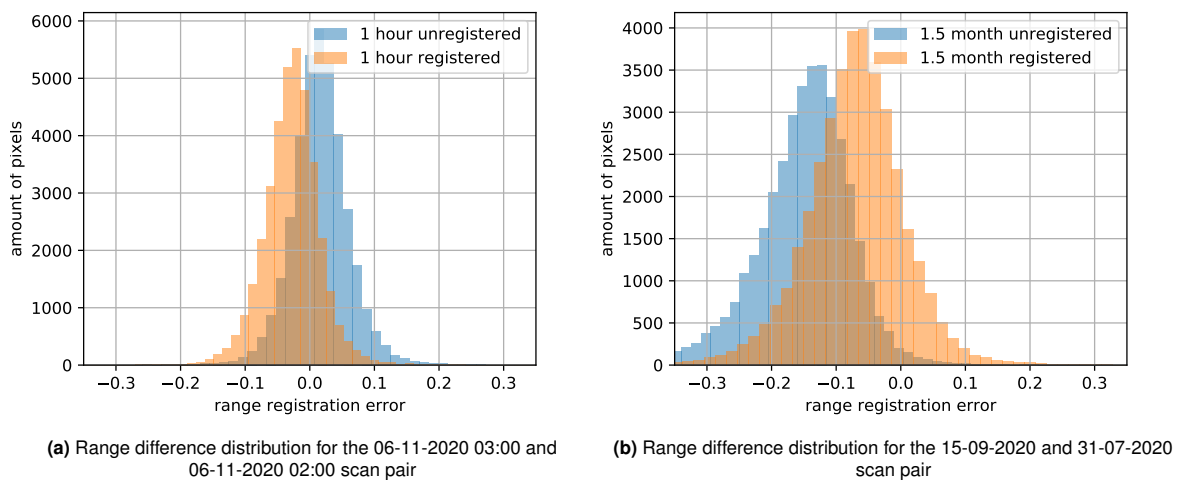


**Figure 5.2:** Histogram of range differences in registered and unregistered range images for two different scan pairs

For the scan pair that is one hour apart, both the mean and standard deviation of the residuals have slightly increased in magnitude after registration. The mean of the residuals has changed sign. Therefore, the applied registration does not seem to improve the quality of the alignment between the two scans 1 hour apart. For the scans that are 1.5 months apart, the effects of registration do seem to be more favorable. The mean of the residuals is halved, indicating better comparability after registration, as no difference is expected. The shapes of the histograms in Figure 5.2 seem to represent a Gaussian function, indicating that the residuals in the analyzed region are normally distributed.

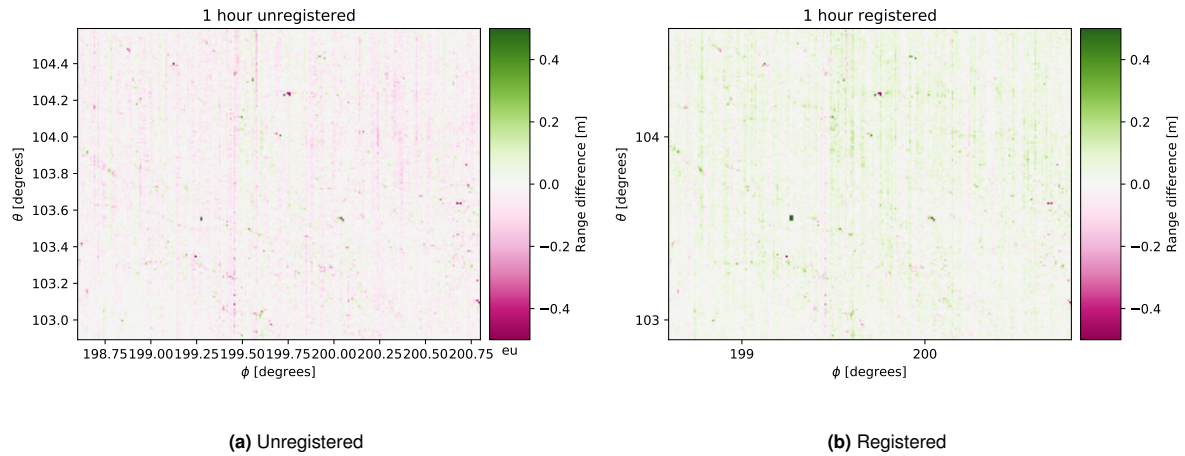


**Figure 5.3:** Observed range difference between scans on 06-11-2020 03:00 and 06-11-2020 02:00.

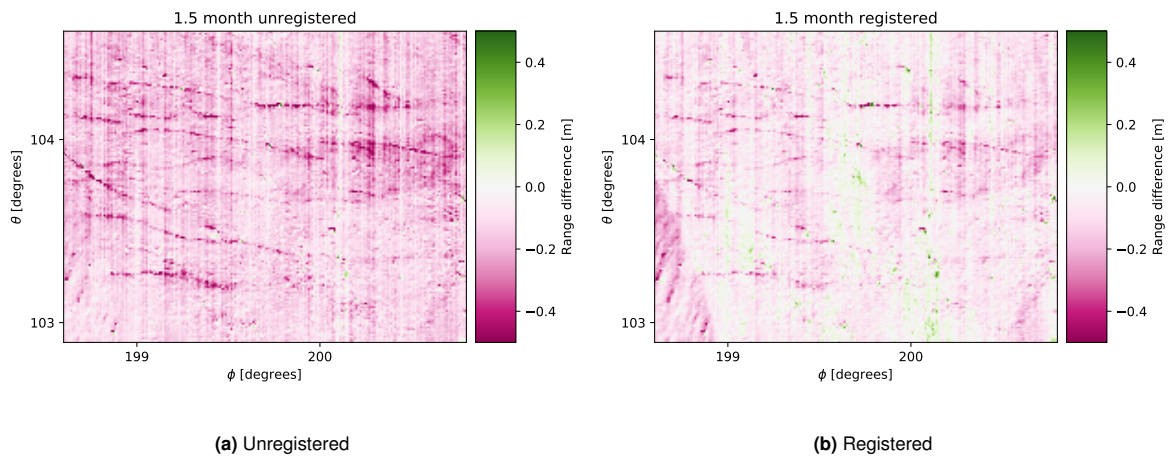


**Figure 5.4:** Observed range difference between scans on 15-09-2020 and 31-07-2020.

### Comparison to point cloud registration

In Figure 5.5 the C2M distances of the 1 hour and 1.5-month scan pair after range image registration, Figure 5.5a, and local ICP registration, Figure 5.5b, are presented. Similar to the results in Figure 5.2, the similarity between the scans in the scan pairs is higher for the 1-hour scan pair. This is the case due to both a larger bias and a larger standard deviation of the C2M for the 1.5-month scan pair. The bias of the C2M after local ICP registration for the different scan pairs is in the millimeter range. The standard deviation is similar for scan pairs of different time scales. The distributions seem to follow a similar distribution to the 1-hour scan pair after range image registration, with a lower bias.

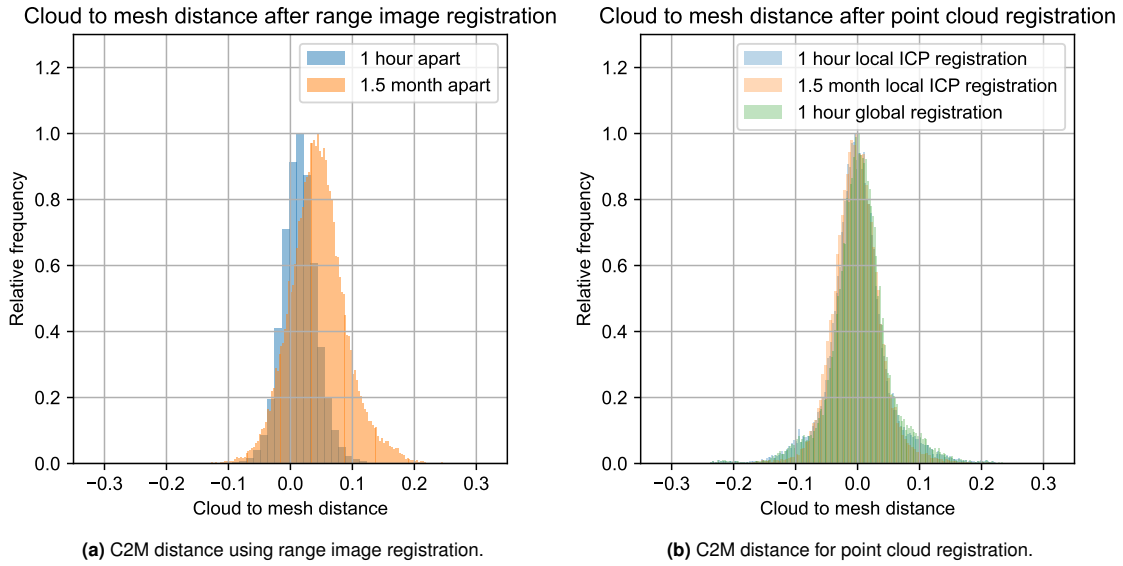


**Figure 5.5:** Histogram of C2M distances using different registration methods.

In Table 5.1 the mean and standard deviation of the C2M distance in the purple region of Figure 3.7 is presented for different registration methods. The local ICP registration and range image registration results correspond to the results of Figure 5.5. The global point cloud registration performed using Riscan Pro results in a lower bias than the range image registration, but this bias is still one order of magnitude larger than that of the local ICP registration.

Registration method	Time span	Mean residual (bias)	Standard deviation
Global point cloud registration	1 hour	0.0044 m	0.049 m
Local point cloud registration	1 hour	-0.00026 m	0.049 m
Range image registration	1 hour	0.0148 m	0.036 m
Local point cloud registration	1.5 months	-0.0014 m	0.040 m
Range image registration	1.5 months	0.044 m	0.046 m

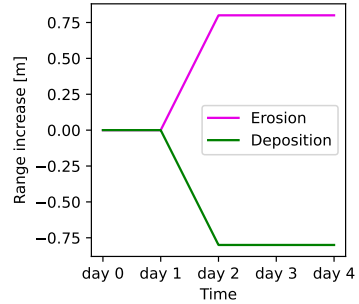
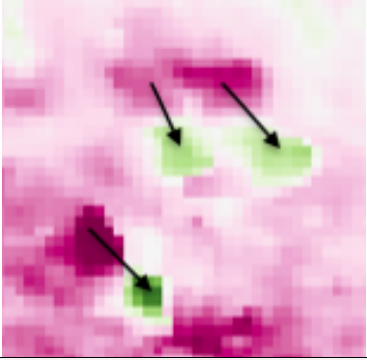
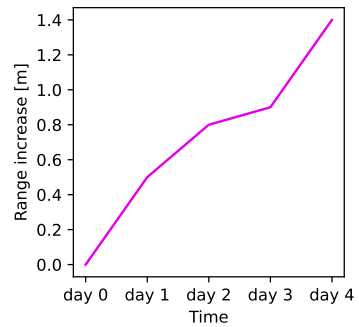
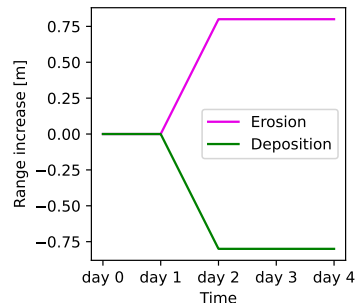
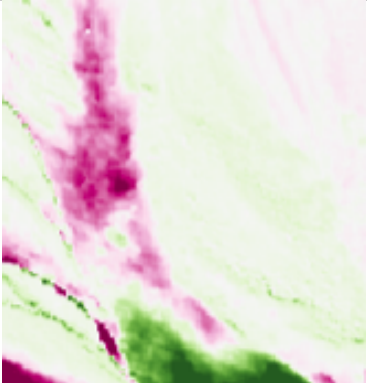
**Table 5.1:** Distribution of C2M distances for different registration methods and scan pairs

After comparison of the range image registration method to the different registration methods, it is found that the range image registration method does not perform better than local or global ICP according to the performance metrics defined in Section 4.2.1. However, the advantages of the automated application of this registration method, and the input for this registration method being raster data, make this registration method most fitting for the chosen set of observations used for analysis in this thesis. Therefore, it is decided that the range image registration method will be applied to summer 2020, 2021, and 2022 observations to create a referenced 4D spatiotemporal data set per year.

## 5.2. Identification of geomorphological processes

Following the range image registration of scans in the summer of 2020 and 2022, A subset is selected which will be used to identify geomorphological processes. The chosen subset spans all available observations per summer, and the spatial extent is provided in Figure 3.7, indicated in yellow. This area is chosen because a large number of cells in this area are subject to surface elevation changes, and the landscape features in this area such as gullies and lateral moraines, indicate the occurrence of varying past geomorphological processes in this area. In this section, areas of interest such as the lateral moraines or gullies refer to the locations indicated in Figure 2.1. First, expected representations of geomorphological processes in the 4D spatiotemporal dataset are shown. Next, the example subsets are presented, after which the PCA is presented in the total area of interest and at the example regions.

To provide an overview of how different geomorphological processes might be represented in the 4D spatiotemporal data, Table 5.2 shows three different locations and difference of range images. A synthetic time series is added to indicate how range observations at a raster cell corresponding to these locations is expected to change over time.

Process and Example time series behaviour	Range difference image	Typical location
<p><b>Sediment transport, rockfall</b></p> 		
<p><b>Dead ice melting, slump</b></p> 		
<p><b>Debris flows, fluvial transport</b></p> 		

**Table 5.2:** Examples of different geomorphological processes, and how these processes are represented in a 4D spatiotemporal dataset

### 5.2.1. Example cases

In this section, three example subsets of the 4D spatiotemporal data set are presented, and for each example subset, the following is shown: The range difference between the last and first observation in the subset, a shaded relief of the region with the cells of the subset contained in a white rectangle, and finally a collection of time series for all cells and observation dates in the subsets, which are coloured according to their cell coordinates. The location of these areas is indicated on the overview image in Figure 3.7 using the numbers 1, 2, and 3.

First, a region with sudden range increases and decreases is shown. Next, an example region showing a steady rate of range increase is presented. Finally, an example of a region with a low amount of range

difference is provided. In Section 5.2.3, the PC loading at these three example areas is presented and discussed.

### sudden range increases and decreases

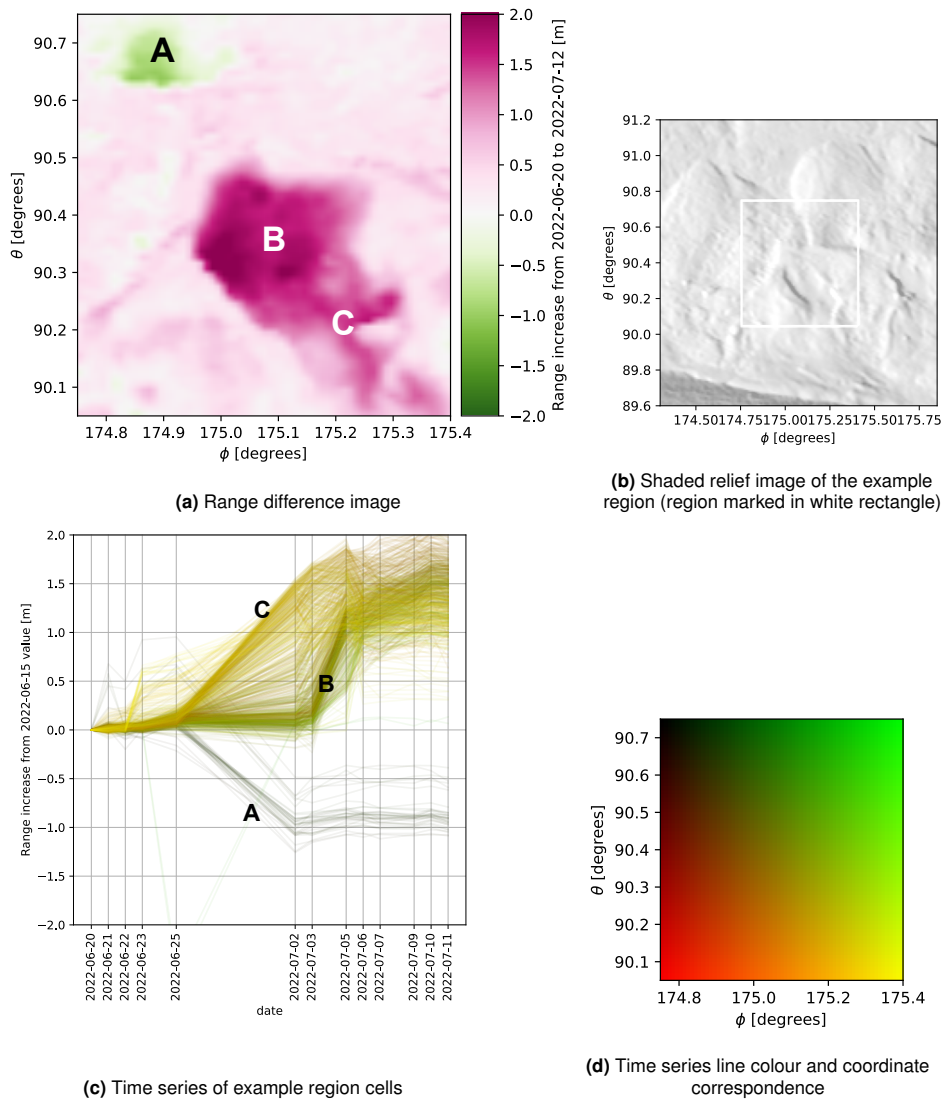


**Figure 5.6:** Sudden range change example subset. Groups of similarly behaving cells are represented with letters A, B, and C.

In Figure 5.6 the range changes in the example region with sudden range changes is presented. Three different large groups of cells showing similar range changes over time exist in this region. A group subject to a range decrease over time can be seen in region A and is represented in the time series by the group of dark lines ending with a negative range increase at the last date of the time series. In the time series plot, it can be seen that the range decrease occurs between the 25 June and 2 July scans. Before, and after this period, the observed ranges in this group do not seem to vary much. Another group of cells with similar range changes is the group of cells in the middle of the region, marked by the letter B. In the time series plot, the ranges of the cells in this group do not vary a lot until the period between 3 and 5 July. In this period, observed ranges increase by around a meter, after which the ranges of cells in this group increase at varying lower magnitudes. The last group of cells showing similar behavior is the group in the lower middle and bottom right region, marked by the letter C. These

cells show a range increase of 1 to 1.90 meters between 25 June and 5 July. After this period, some of the cells decrease in range, whereas others do not change.

### Steady range change

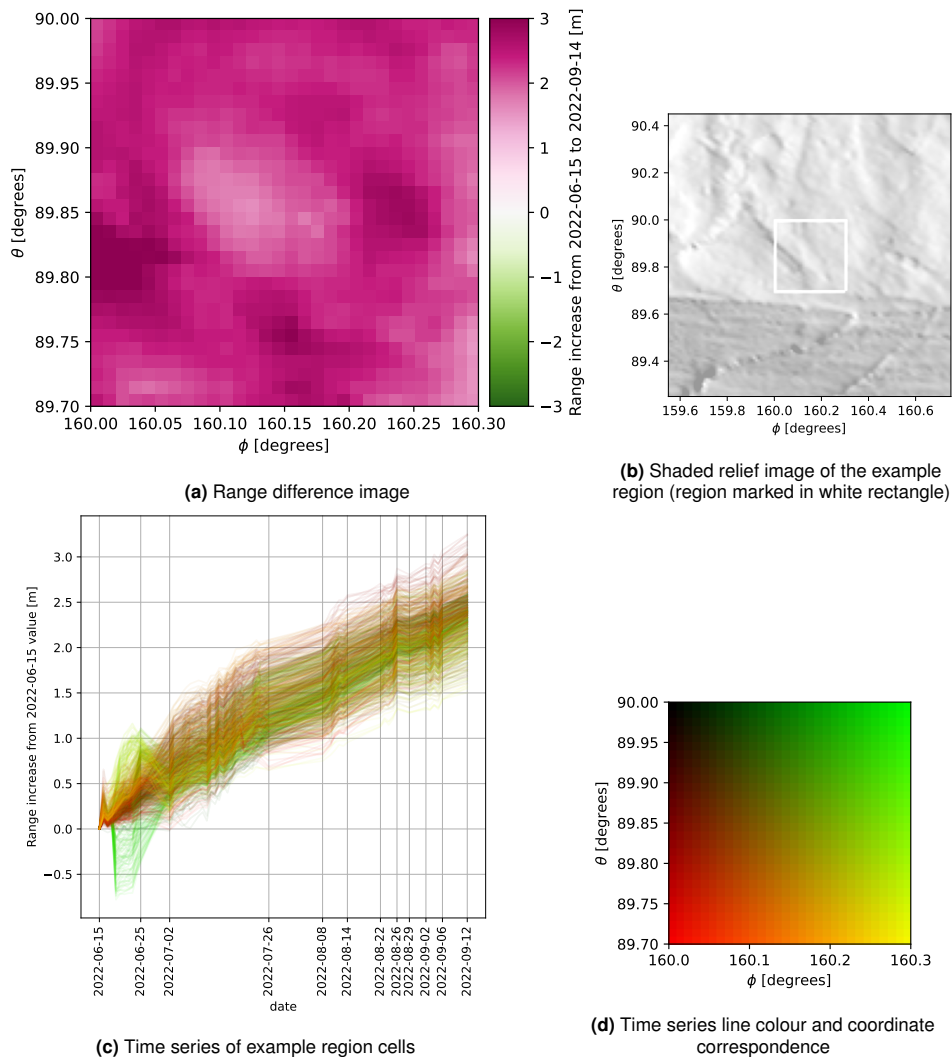


**Figure 5.7:** Steady range change example subset.

in Figure 5.7, for most cells, a range increase between 1.5 and 3 meters occurs over the observed period. The majority of the cells show a range increase at a steady rate. Two groups of cell time series deviate from this behavior. From 18 June to 2 July, one group of cells shows a sudden range decrease, followed by range increases at higher rates than the linear trend of the region. In the other deviating group of cells, at the same dates, a sudden range increase can be seen, after which the range decreases.

### Little range change

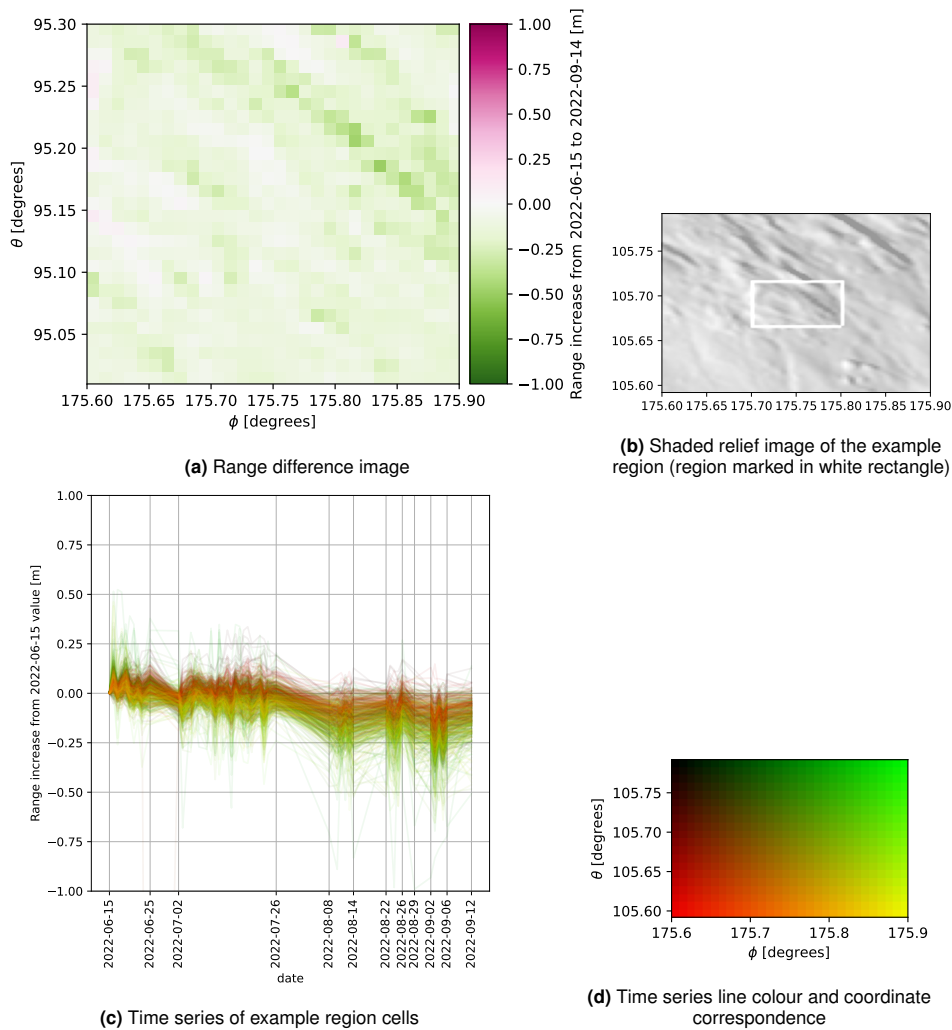


**Figure 5.8:** Little range change example subset.

In Figure 5.8, the range changes in a region with little range change are shown. The range change between the beginning and end of the observed period is a few decimeters. From scan to scan, observed ranges can change a few decimeters as well. Magnitudes of differences seem to be related to the incidence angle, as some features of the shaded relief image can be recognized in the range difference image in Figure 5.8a.

#### 5.2.2. Small magnitude change

In this section, the results of the low variation change analysis of Section 4.4 are presented.

In Figure 5.9, the mean range difference between the first 10 and last 10 observations, and for a 40 by 40 cell neighborhood means of the 2020 4D spatiotemporal dataset are presented.

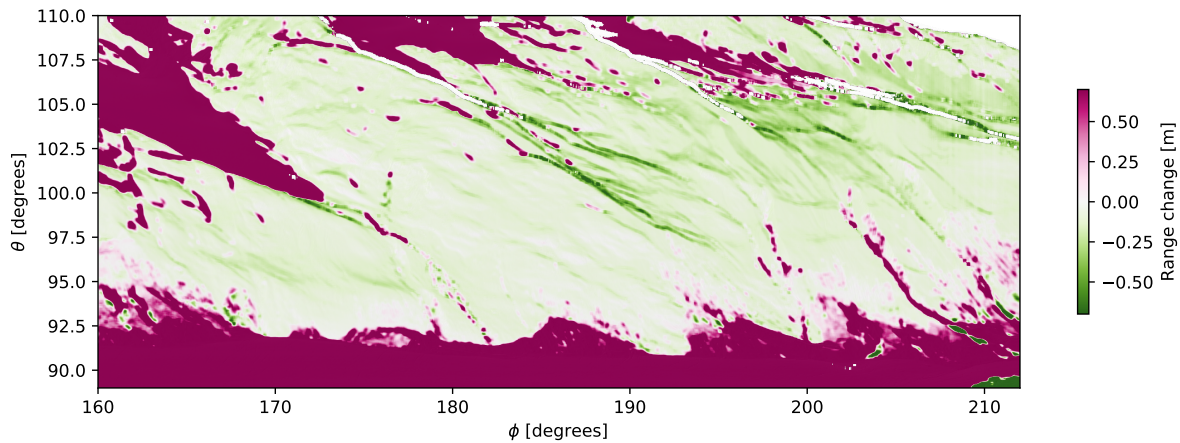


**Figure 5.9:** Spatial and temporal average difference between first and last 10 scans of summer 2020.

In Figure 5.10 the mean range change is shown with similar temporal and spatial aggregation as the above figure.

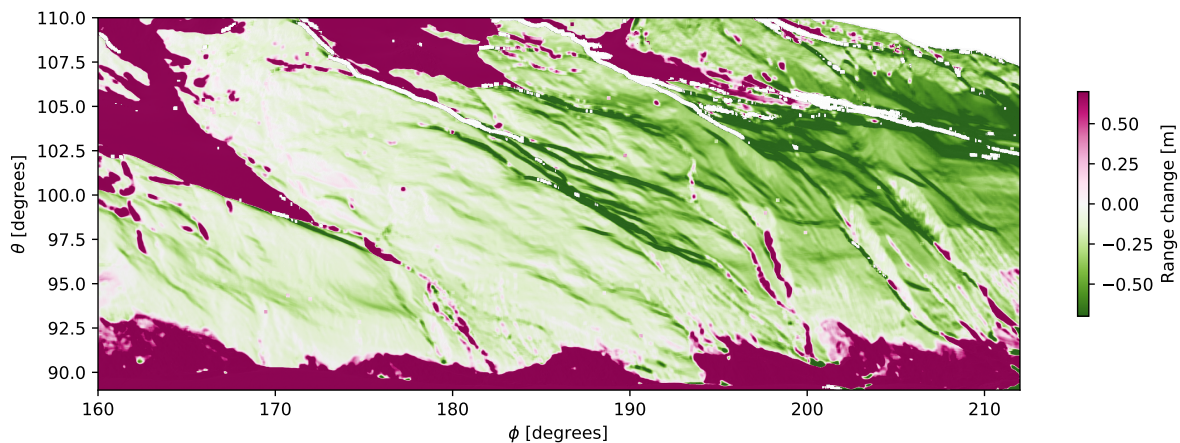


**Figure 5.10:** Spatial and temporal average difference between first and last 10 scans of summer 2022.

### 5.2.3. Principal components

Following the steps provided in Section 4.5, a set of principal components are computed, describing the range changes of the 2022 summer in the yellow area in Figure 3.7. The PC loading is plotted corresponding to the cell locations, and the PC scores are plotted against the represented observation dates. First, the eigenvalue spectrum of the PCs is presented. Next, the loading and scores of the (combined) PCs as well as the choice of PC combinations are discussed. After, the false colour image of the first PCs loading is presented, after which the loading of the PCs at the different example areas of Section 5.2.1 are presented and compared. Finally, the PCs from the summer 2020 dataset are presented and compared to the summer 2022 PCs.

#### Principal component eigenvalue spectrum

The eigenvalues belonging to each principal component are shown in Figure 5.11. The sampling error is computed using North's rule of thumb with a population size of 50 (the number of observations). Belonging to each PC, the error range is indicated with blue triangles. The first two PCs are well separated and their sampling errors do not overlap. The first four eigenvalues are significantly larger than the following, and thus explain nearly all variance in the dataset. The third and fourth principal components do seem to be very close, indicating an effectively degenerate multiplet (North et al., 1982). Therefore, it is chosen to analyse relations of a linear combination of the third and fourth PC instead of analysing these PCs separately.

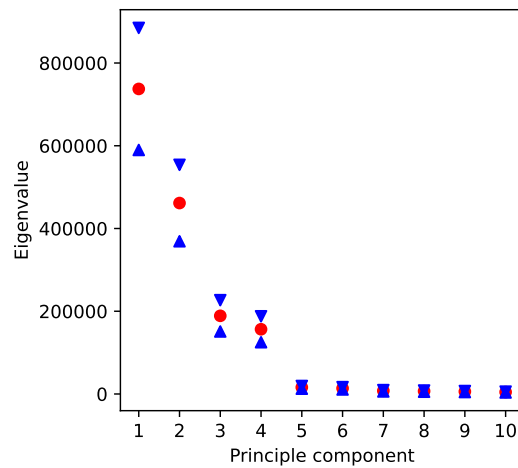


Figure 5.11: Eigenvalues of the computed PCs. Sampling error estimates are indicated with blue triangles.

### Principal component 1

In Figure 5.12, the first PC is presented. This component explains the largest amount of variance in the used data set. The loading of the PC is largely positive at the lateral moraines. Negatively loaded regions largely occur in the slopes located between gullies. around the meltwater stream at  $(\phi, \theta) = (180^\circ, 93^\circ)$ , areas of both positive and negative loading to the PC alternate each other at low spatial scales. Furthermore, in gullies, regions of both positive and negative loading can be found. At the bottom of some gullies, regions of negative loading are present.

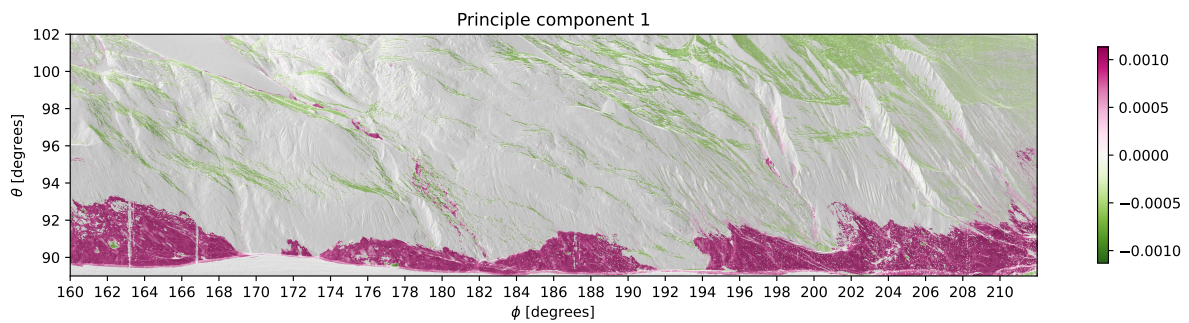


Figure 5.12: 2022 principal component 1 loading per cell, overlaid by a shaded relief image. Green and pink indicates negative and positive correspondence to the PC, respectively. Color saturation corresponds to the magnitude of the loading.

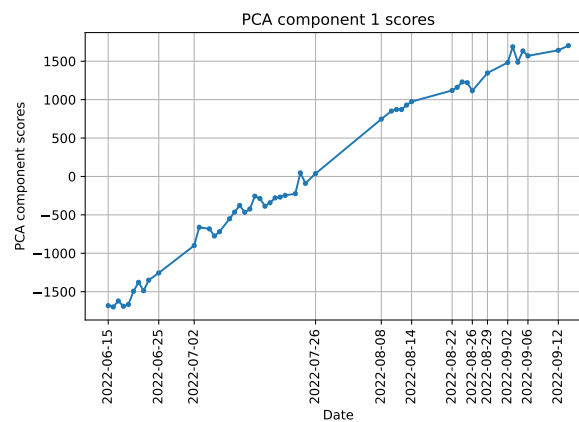


Figure 5.13: 2022 Principal component 1 scores.

Consider the scores per observation for PC 1 in Figure 5.13. The behavior represented in the scores of the component seems to correspond to a linear increase of the observed range over time, with a slightly lower rate of change after 14 August. When looking at the loading of this PC in Figure 5.12, it can be seen that the range changes of most cells correspond to this linear behavior. As the linear trend of the PC scores is positive, this represents an increase in range over time. Zones of mostly positive loaded cells such as the lateral moraines are thus subject to processes that increase the range between the objects and the scanner over time. As the lateral moraines are sloped, this range increase could be caused by a lowering of the lateral moraines. An explanation for this lowering at a steady rate of the lateral moraines during summer could be the thawing of ice located underneath the surface of the lateral moraines, which can be the cause of lateral moraine reworking (Porter et al., 2019, Betz et al., 2019).

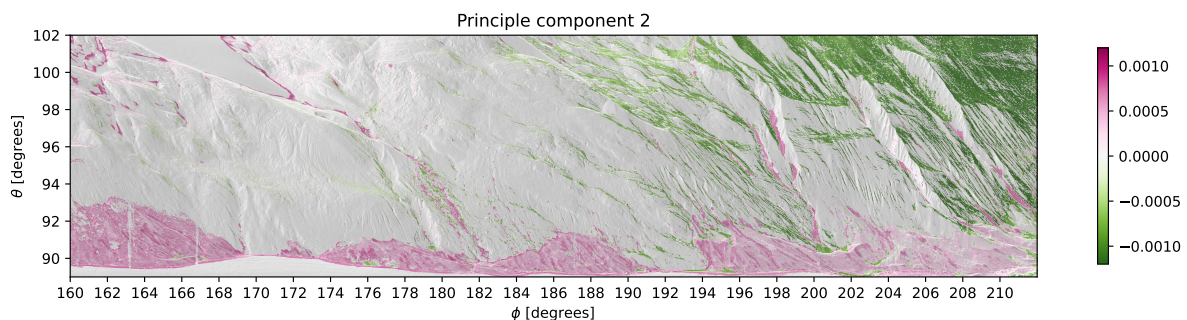
The alternating pattern of positive and negative loads along the meltwater stream at  $\phi = 180^\circ$  may be the result of the reworking of sediment in these areas at steady rates. The zones of positive loading, where the range steadily increases over time, could indicate regions of sediment source. Zones of negative loading could indicate zones where material is deposited. An explanation for the correspondence to a steady change in these regions could be the meltwater stream which is present throughout the observed period, as fluvial processes modify landforms at the margins of these streams (Porter et al., 2019).

Some patches located on the lateral moraines are negatively loaded in this PC, which could indicate that material is deposited in these areas over the observed period. Material deposited in this area could originate from the positively loaded areas directly above these patches. Processes that could cause this reworking at steady rates could again be related to ice melting.

In the gully, located at  $\phi = 198^\circ$ ,  $\theta = 95^\circ$  in Figure 5.12, a group of cells with strong positive loading is present. This could indicate that erosion of the gully occurs at a steady rate in these regions. However, when looking at the range time series at this location, the total change in this area seems to result from changes occurring over a few days, with periods of little change in between. The behavior is better represented by a small number of sudden changes rather than changes at a steady rate. Therefore, the behavior of these cells are not similar to for instance the cells on lateral moraines as shown in Figure 5.7c, which correspond largely to the scores of this PC. This indicates that it can not be assumed that the cells with significant loading in this PC are all subject to processes with a steady rate of surface elevation change.

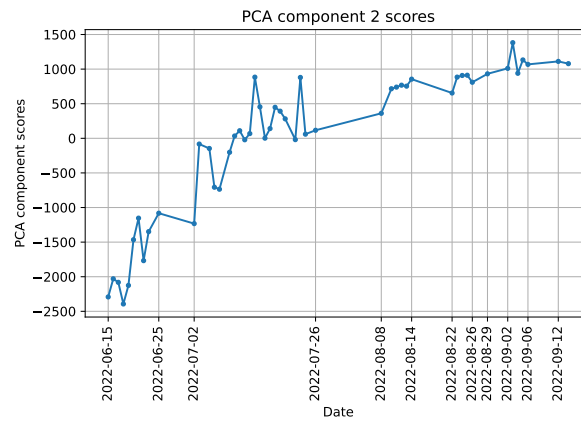
### Principal component 2

Figure 5.14 shows the loading for the second PC. Again, in the region around  $(\phi, \theta) = (180^\circ, 93^\circ)$ , areas of negative and positive loading alternate. This effect is also visible at some parts of the lateral moraines, where mostly a small magnitude positive loading occurs. In the area on the higher slopes on the left side of the image, also positive loading occurs. The higher slopes on the right side of the image correspond negatively with a strong magnitude to the second PC. Gullies mostly contain regions with positive loading.



**Figure 5.14:** 2022 principal component 2 loading per cell, overlaid by a shaded relief image. Green and pink indicate negative and positive correspondence to the PC, respectively. Color saturation corresponds to the magnitude of the loading.

The scores of the second PC are presented in Figure 5.15. The pattern of the scores in this PC seems to be represented by a range increase at varying rates until just before 26 July. After 26 July the range decreases until 8 August and remains similar for the remaining time.



**Figure 5.15:** 2022 Principal component 2 scores.

When looking at the scores corresponding to the second PC, the signal is less linear than the first PC. This complicates the interpretation of the relations that are described in this PC. A possibility could be that the scores represent a strong range increase for the period up to around the end of July. The cells with a high loading of this PC are located around the gullies and on the lateral moraines, as well as around the cirque glacier. The highest magnitude loading occurs at the gullies and intergully slopes on the right side of the analysed region. In combination with the slightly negative loading in the first PC, this could indicate a movement of these slopes towards the scanner, which is further discussed in Section 6.3. Along the meltwater stream, at a lower magnitude, similar patterns of loading occur as for the first PC. However, the locations of positive and negative loading are not the same as in the first PC. This change could indicate that both deposition and erosion around the meltwater stream occur at the same locations within the observed period. Because of the little change in the scores surrounding the two sudden change event periods, the reworking of materials portrayed in this PC is likely caused by fluvial processes of the meltwater stream.

The steady change example region does show positive loading to the second PC. This is expected as the PC scores show a range increase over time. When looking at the range change of this example region, apart from the linear trend, some high-frequency fluctuations around this trend exist for all cells. It could be that these fluctuations correspond to the fluctuations present in the second PC scores.

### Principal components 3 and 4 combined

Because of the third and fourth PC forming an effectively degenerate multiplet, the relations in the original data are randomly mixed within the PCs (North et al., 1982). Any linear combination of the PCs in a degenerate multiplet is also an empirical orthogonal function (principal component) (North et al., 1982,) so it is chosen to combine these two PCs into a new PC. In Figure 5.16, the loading of the combined third and fourth PC is shown. A linear combination of this combination was chosen, such that the scores corresponding to the PC represent two range increase events. The original PC scores represented mostly only one of these range increase steps (The third and fourth PC scores represented the second and first sudden change event, respectively).

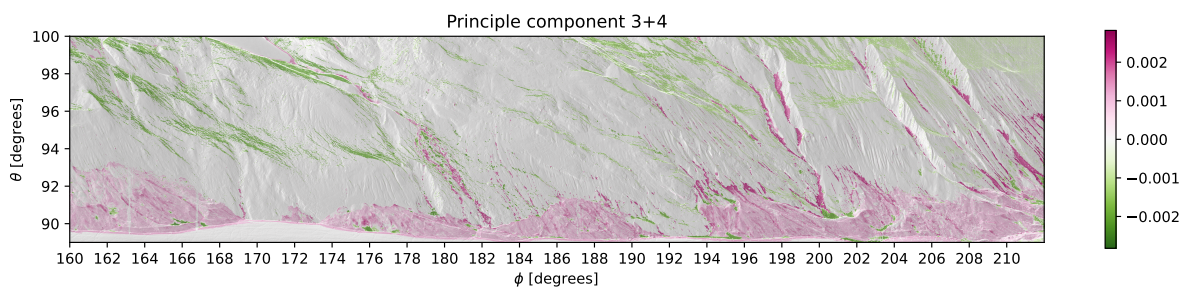


**Figure 5.16:** 2022 principal component 3 and 4 loading per cell, overlaid by a shaded relief image. Green and pink indicates negative and positive correspondence to the PC, respectively. Color saturation corresponds to the magnitude of the loading.

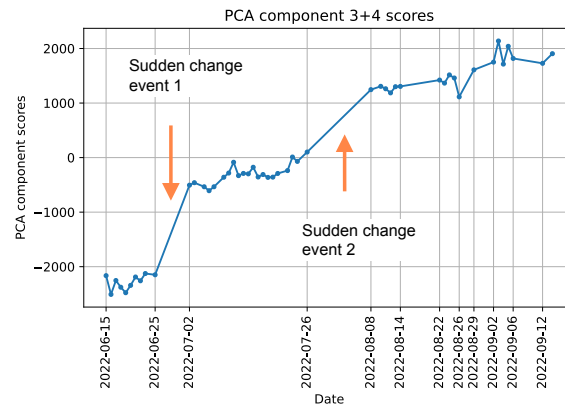


**Figure 5.17:** 2022 principal component 4 scores, with two sudden change events indicated.

The scores of this combined PC, shown in Figure 5.17 are defined by two events of significant range increase. As seen in Figure 5.17, the first event occurs between the 25 June and 2 July scans. The latter between the 26 July and 8 August scan. On 27 and 28 June, the heaviest precipitation event of the observed period occurred, as recorded by station Hintereis (“Hintereis station precipitation data”, 2022). When looking at the spatial distribution of the loadings in Figure 5.16, it can be seen that positive loadings mostly exist along the lengths of the gullies or other concave features. Negative loadings exist mostly at the bottom of these features. This pattern suggests that material is eroded from gullies, and deposited at their foot, causing the range to increase in the gullies and decrease at their bottom. Gully modification has been linked to debris flows or fluvial transport caused by high-magnitude precipitation events (Dusik et al., 2019). Between 26 July and 8 August, air temperatures reached 15 degrees Celsius at the Im Hinteren Eis weather station (“Im Hinteren Eis station precipitation data”, 2022), and again precipitation occurred on several days. These events could cause an increase in the thawing of ice and resulting reworking of lateral moraines (Porter et al., 2019), which could explain the positive loading of most lateral moraine cells for this PC. The loading of the combined PC at the steady change example region is of small positive magnitude. In the sudden change example area loading of the combined PC provided in Figure 5.20, large loading occurs for the regions A and C as indicated in Figure 5.6 in Section 6.3. This result indicates good isolation of these two sudden change events from other signals through the PCA, as these sudden changes occur between the 25 June and 2 July scan, which corresponds to the first sudden change of the combined PC, shown in Figure 5.17.

### False colour representation of PC loading

In Figure 5.18, for each location the PC contributing most to the behavior is shown. Groups of cells with similar loading in the three different PCs are easily identified due to their similar colour in this image. On the lateral moraines, the reddish shade indicates high correspondence to the first PC. The colour of the lateral moraines becomes redder for increasing horizontal scan angles. This suggests that cells on lateral moraines with higher  $\phi$  (around the glacier tongue) show more linear behaviour than cells on lateral moraines at low  $\phi$  angles which are adjacent to the glacier. Furthermore, on the moraines, patterns of different colour regions exist, indicating homogeneous change behaviour on these objects. For instance, groups of blue cells indicate regions where change is mostly related to the sudden change events represented in the third and fourth combined PC. Along the meltwater stream, zones of different colours are present, indicating that the surrounding of this stream is reworked with a large variation of change behaviour. Other interesting features in this image are the purple and green zones on the left side of the image and the intergully slopes, respectively.

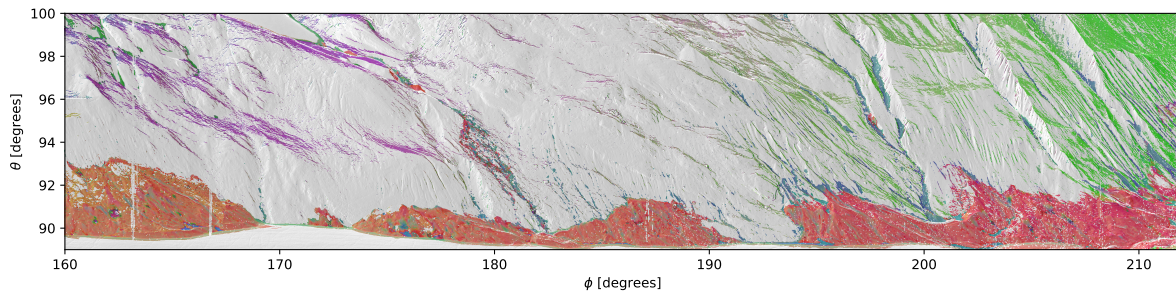


**Figure 5.18:** False colour image of the relative loading (as described in Section 4.5) per raster cell for the first three (combined) PCs of the 2022 data set. Red, green, and blue correspond to the first, second, and 3 and 4 combined PC, respectively.

### Principal component loading in example areas

In this section, the loadings for the first four PCs are provided for the regions corresponding to the example subsets presented in Section 5.2.1.

In Figure 5.19, the loadings of cells in the steady range example region are presented. It can be seen that all cells in this region are of high load in the first PC, which is as desired as this PC corresponds to linear change. The loading of the cells is most heterogeneous in the combined PC.

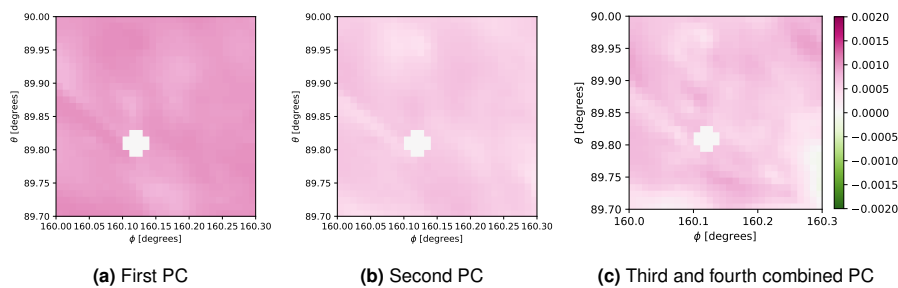


**Figure 5.19:** 2022 principal component loading for the steady range change example region

In Figure 5.20 The loading in the sudden change example region is shown. The highest loading in this region occurs in the third and fourth combined PC, for the two different regions subject to a large range change between two scans, as described in Section 5.2.1. This is as desired as in the A and C area indicated in Figure 5.6, sudden change occurs over the first event represented in the PC scores of the combined PC in Figure 5.17. The B region is not loaded with high magnitude in the first three PCs, for which the reason is discussed in Section 6.4.

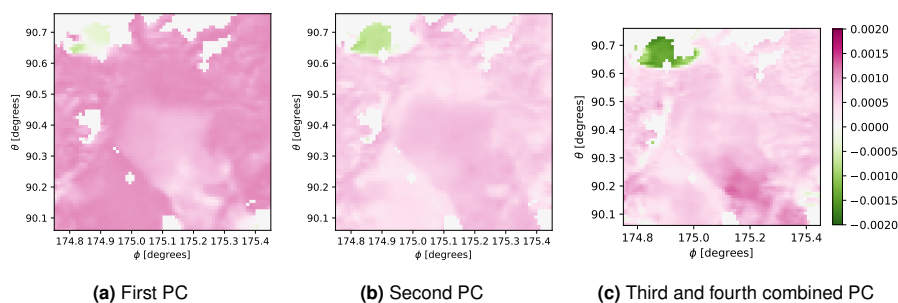


**Figure 5.20:** 2022 principal component loading for the sudden change example region

The loading of the first PCs at the little change example region is shown in Figure 5.21. A part of the cells in this region have been masked out for the PCA because of a low standard deviation in time. The remaining cells are mostly of high load in the combined PC. In the first component, these cells are also loaded, but with less magnitude. In the second PC, the cells in this region are not significantly loaded.

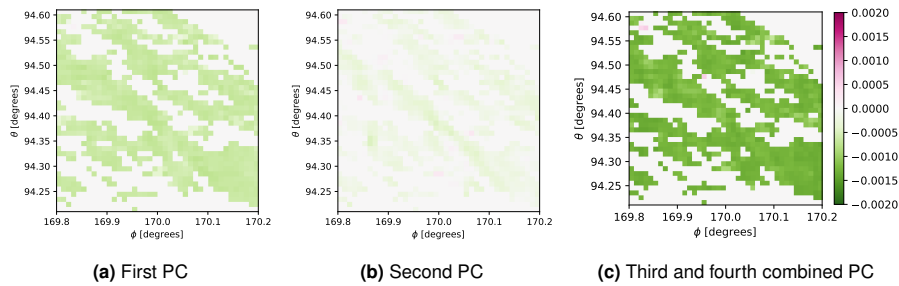


Figure 5.21: 2022 principal component loading for the little change example region

### Summer 2020 principal components

The scores of the PCs computed for the summer 2020 data set are provided in Figure 5.23. The first 2020 PC scores represent a similar behaviour to the first PC scores of the 2022 dataset, which is also reflected in the similar loading patterns of these PCs, as shown in Figure 5.22.

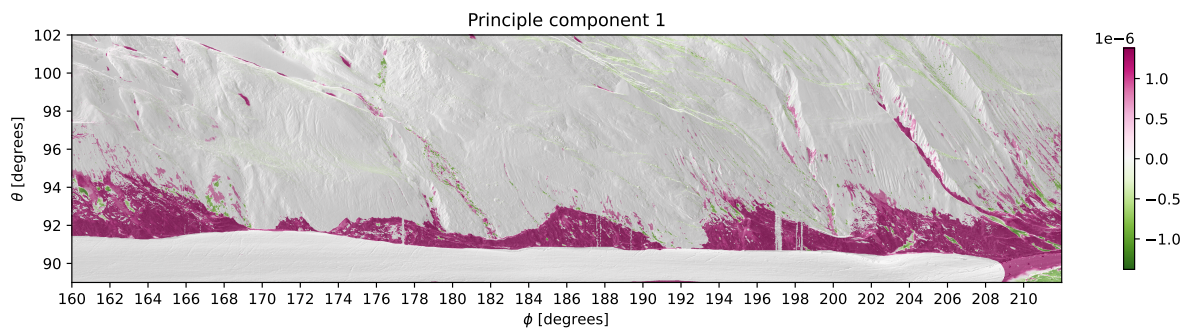


Figure 5.22: 2020 principal component 1 loading per cell, overlaid by a shaded relief image. Green and pink indicates negative and positive correspondence to the PC, respectively. Color saturation corresponds to the magnitude of the loading.

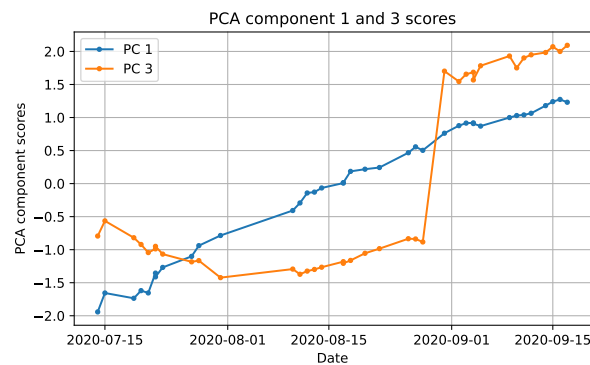
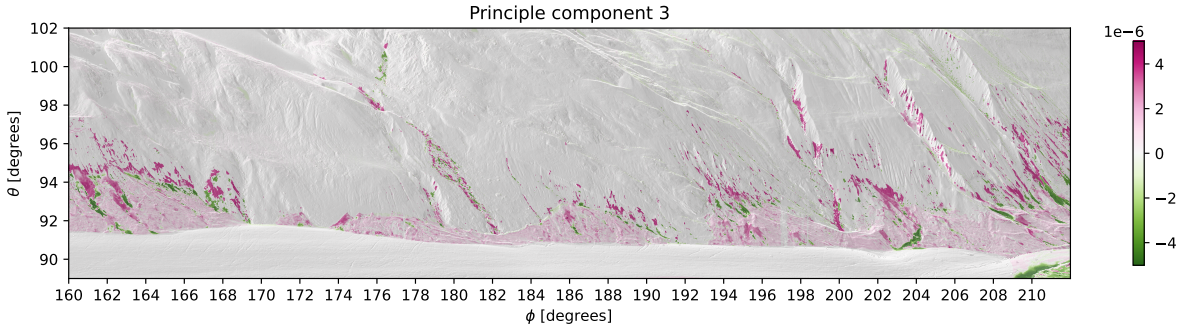


Figure 5.23: 2020 principal component 1 and 3 scores.

The scores of the 2020 third PC represent a large range increase between two scans at the end of August. The corresponding loading of this PC, presented in Figure 5.24, shows patterns of alternating regions of positive and negative loading on and around the lateral moraines, as well as in the gullies. These patterns indicate erosion and deposition occurring at the end of the August range increase event.



**Figure 5.24:** 2020 principal component 3 loading per cell, overlaid by a shaded relief image. Green and pink indicate negative and positive correspondence to the PC, respectively. Color saturation corresponds to the magnitude of the loading.

# 6

## Discussion

In this chapter, the methods and results are discussed and compared. First, the results regarding the range image registration are discussed in Section 6.1. Next, complications of the time series creation and possible causes are considered in Section 6.2, after which the low magnitude change analysis results are linked to causes different from surface elevation change in Section 6.3. In Section 6.4, different aspects of the PCA method are discussed and compared to different methods of analysing PLS data. Finally, in Section 6.5, potential research topics utilising the IHE PLS system are considered.

### 6.1. Range image registration

In this section, methods and results regarding the creation of range images, as well as their registration method are discussed.

#### Registration reference areas

From the results presented in Figure 5.1, it can be seen that the registration method using the mountain ridges as a stable reference area performs slightly better when registering scans with a longer time interval between the scans compared to using the point cloud and webcam stable objects. This difference in performance could be caused by the fact that even though in the point cloud and webcam analysis, the other regions seemed stable, only two epochs were used to draw this conclusion. Therefore, these regions could be subject to change whereas this did not seem to be the case in the used scans.

Another reason for this difference could be that there is a larger reference area using the mountain ridges. More key points are found due to the larger area, which results in a larger redundancy in the calculation of the transformation between two scans. Not only the area of the mountain ridges but also their stronger geometry could be more favorable for creating reliable key points compared to the regions identified using point cloud and webcam image analysis. In Figure 3.7, a larger contrast and more change at low spatial scales seem to be present in the mountain ridges. Both factors could benefit the creation of reliable key points.

Besides a difference between the regions used for registration, it can be seen that the mean absolute range difference increases for increasing time intervals between the registered images for both registration methods. A possible cause for this increase can be caused by actual changes in the scanned geometry in the area used to compute the range difference. It can not be assumed that no changes are occurring in this area. Over longer time intervals, the influence of these actual changes will increasingly change the topography and thus result in a larger mean absolute range difference. Another cause for this effect could be changes in the reference zones, which would result in an ill registration of the scan pairs due to changes in the key point positions relative to each other. This change is not more likely than the previously mentioned effect, because it occurs using both reference zones, and key points with range changes in their proximity are filtered out in the registration procedure. Furthermore, for surface elevation changes to influence the registration, they would need to be distributed over the reference areas with either a spatial trend or a constant value. Otherwise, with a random distribution and zero mean distribution of surface change in the reference areas, influence on the registration would be little

due to the redundancy in the number of key points.

A more likely factor influencing the mean absolute range difference increase for larger time intervals could be errors due to the measurement system. Changes in atmospheric conditions could contribute to errors with a constant or trend spatial distribution. Furthermore, the scanner position could slightly change over longer time scales, which influences registration quality as discussed in Section 6.2.

### **Before and after registration comparison**

The histograms in Figure 5.2 show that the automated range image registration approach does not always improve the alignment of two observations. In the case of the 1-hour separated scan pair, the scans do not seem to align better after registration, as the magnitude of both the mean and standard deviation of the range difference does not significantly change. By looking at the spatial distribution of residuals in Figure 5.3, the largest magnitudes of range difference seem to represent the scan line patterns as identified by Voordendag (Voordendag et al., 2021). Before and after registration, the locations and signs of the most notable scan lines changed. Likely, the scan line effects are present in every column and performing the registration results in the residuals of different scan lines becoming the more notable residuals. This effect could occur due to a bias in the range difference before and after the registration. Because the sign of the bias is changed, the largest magnitude range differences will now occur on the other side of the ground truth. Some outliers are present in the range difference image after registration.

The visibility of the scan lines in the range difference images could indicate that the largest influence on the range difference error between the two scans is from the scan line effect caused by the motion of the scanner. Although a more elaborate analysis would be needed, this does provide some insight into the uncertainties of the range observations. Based on the residuals, uncertainty with a standard deviation of around half a decimeter can be expected for this area under favorable conditions.

In the case of the 1.5-month separated scan pair, the registration does seem to improve the alignment of the observations. This improvement is mainly visible due to the reduced magnitude of the mean residual after registration. When looking at the spatial distribution of the residuals in Figure 5.4, again the residuals seem to correspond to scan lines. Before registration, there is a negative bias which is reduced after registration. In a range difference image, if two images are not perfectly aligned, the topography of the observed region can be recognized as explained with gullies as an example in Section 4.2.2. Before registration, a misalignment in the vertical direction results in range differences for locations with a large range gradient in the vertical direction. This effect is reduced after registration. However, for locations with a range gradient in the horizontal direction, such as the gully edge in the lower left corner of the image, this effect did not decrease in magnitude. Before registration, the gully edge could not be distinguished from the range difference image, whereas after registration, this is the case. Therefore, it is clear that alignment after registration is not perfect because residuals still depend on viewing geometry.

### **Comparison to point cloud registration**

The most prominent difference between the different registration methods presented in Figure 5.5 and Table 5.1 are the differences in the mean C2M distance of different registration methods. Using the ICP algorithm on the analyzed subset of the total scan (purple zone in Figure 3.7), a bias of less than a millimeter is achieved. For the global point cloud registration of the 1-hour scans, this bias is of a few millimeters, and for the range image registration, this bias is in the centimeter range. A key influence on the low bias after local ICP registration could be the fact that this registration is based only on the data in the analyzed area. For the global point cloud registration and range image registration, the alignment of the point clouds is based on the total point cloud and the mountain ridges' key points, respectively. Thus, these methods aim to minimize a much larger and more varied area than in the case of the local ICP registration. Therefore, it can be expected that on smaller subsets of the globally registered point clouds, a larger bias is present.

## 6.2. Time series creation and examples

For the scans of summer 2021, it was not possible to register a range image from before 7 September 2021 to range images after this date. This is likely caused by a change in the scanner position. During a visit to the scanner on 7 September, the position of the instrument changed a few centimeters. When the position of the scanning instrument changes, the spherical coordinates of objects will change. For objects with a large distance from the scanning instrument, this effect will likely be small. However, for objects closer to the scanner, this effect will be larger and a shift with a magnitude of multiple raster cell sizes can be expected. Due to this effect depending on the distance to the scanner, a spatial relation will exist for the coordinate shift caused by the scanner position change. This effect is also schematically depicted in Figure 6.1. Because this effect will cause an error with spatial trends for a large number of key points, the registration method will not be able to find a transformation between two range images that will result in a low error across the range image. Therefore, the scans of 2021 are not converted to a 4D spatiotemporal data set. This error shows that for the registration method to properly function, no shift in the scanner position must occur from scan to scan. This requirement negatively impacts the scalability of this registration method to different observation setups, as in multiple PLS setups, the scanning instrument position is found to vary between scans (Kuschnerus et al., 2021a; Voordendag et al., 2022). However, by estimating the translation of key points that occurred due to scanner movement, the registration method could be improved so it can be used in PLS systems where a slight position change might occur.

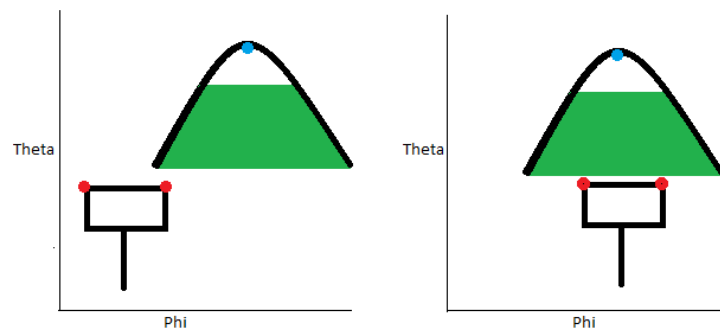


**Figure 6.1:** Exaggerated representation of the influence of position change on the coordinate relation between key points at different distances from the PLS instrument. Red dots represent key points of a nearby object, the blue dot represents a key point on a faraway object. The position of the blue and red key points change at different scales in the image coordinate frame due to a change in the instrument position.

## 6.3. Small magnitude change

The small magnitude range changes are presented in Figure 5.9 and Figure 5.10. In these figures, a slight range decrease is shown for the slopes above the lateral moraines and around the gullies. In 2020, the magnitude of this change is a few centimeters excluding regions affected by large incidence angles (which lead to higher magnitude range change as described in Section 4.2.2). Because in these figures, the mean of the first 10 scans is subtracted from the first 10 scans mean of summer 2022, the registration error must be either very large in a few scans, or present in multiple scans within one of these two sets of range images. When viewing the time series from the little change example region, presented in Figure 5.8, it can be seen that indeed, before 26 of July, range values deviate around a different value than after this date, so a more consistent change of range occurred. After this scan, heavy precipitation and temperature fluctuations occurred. Range change due to this event could have two possible causes.

The first cause could be the reworking of material on the slopes as a result of this weather event. However, the range increase indicates the deposition of material on these slopes. In this case, patterns of erosion indicating material source locations should be present above all slopes with a range decrease, which is not the case for all slopes. The other possible cause for the range change after July 26 is a slight change in the scanner position or the position of reference objects as a result of the weather

event. In this case, a situation could occur in which the registration method is incapable of providing a proper alignment as discussed in Section 6.2. The mean range difference is larger for objects further away from the scanner. This indicates that the observed range differences are the result of a consistent registration error, as for these objects, the ground sampling distance is larger than close-by objects, resulting in higher magnitude errors as a result of misalignment for nonzero incidence angles.

Because the range decrease is also visible in the 2020 data, there could be a contribution of effects such as changes in atmospheric conditions. To rule out the possibility of actual surface elevation change occurring, an analysis using point clouds could be performed, and atmospheric conditions at the first and last 10 scans of the 2020 and 2022 summer could be investigated to see if consistent changes occur. Another option would be to measure surface elevation changes in these slopes using a different system such as synthetic aperture radar, differential GNSS, or UAV-LiDAR, and compare the results to the measurements from the PLS system.

## 6.4. Principal component analysis

In this section, different aspects of the PCA methodology and results are discussed, and compared. First, the high frequency fluctuations in the second PC of 2022 are discussed. Next, the effects of domain dependence of the PCA results are discussed. After, the false colour PC image is discussed. Next, the PCA of different years is compared, after which the PCA method is compared to other methods of summarising 4D spatiotemporal data. Finally, the potential of the PCA method for other PLS systems is discussed.

### Fluctuations in the second principal component

High-frequency fluctuation of the scores could be a result of misalignment errors, which occur from scan to scan. However, if these fluctuations could be caused by misalignment, the magnitude and sign of loadings of this PC would be dependent on incidence angles, which is not the case. Another explanation could be that for most cells in the analysed area showing a linear trend, the observed range change is not perfectly linear. Therefore, fluctuations around this linear trend could be represented in the scores of this PC. The fluctuations of the second PC scores correspond to smaller scale fluctuations around the linear trend in the first and fourth PC scores. A cause of these fluctuations could be variations in meteorological conditions in the atmosphere between the scanning system and the analyzed area. Changes in air temperature, air pressure, and water vapour pressure change the group velocity of a laser pulse (Voordendag et al., 2021). one degree of air temperature change, results in an observed range change of 1 particle per million (Voordendag et al., 2021). At an observation distance of more than two kilometers, a temperature change of 5 degrees results in a range error of 1 cm if the range is assumed constant. Combined with the effects of air pressure and vapour pressure change, the atmospheric influences could alter the range observations in the analyzed area up to a few centimeters. These fluctuations do not occur for all cells in the region because both positive and negative loading is present in the PC. It would be most likely that in the case of atmosphere influence, negative loading regions correspond to the fluctuations because these regions are furthest from the PLS, and loading magnitude increases with distance from the scanner. To prove this hypothesis, an elaborate analysis of the relation between range changes in these areas and atmospheric conditions should be performed.

### Obscuring of small scale events

Notably, the B region indicated in Figure 5.6 is not highly loaded in any of the first three (combined) PCs. This could be explained by the fact that the B change event occurred at a different date than most other sudden range change events in the data set, which mostly occur on one of the change events isolated in the combined PC. This is an example of a disadvantage of the PCA technique in isolating change events, as the smaller variance changes end up in higher-order PCs, which might not be inspected or included in a reconstructed signal. The cause of this effect is the dependence of the computed PCs on the chosen subset of data. If a smaller subset is chosen, then the variance of a small range change event becomes a larger portion of the total variance than in the case of a large subset of data. As a result, the first PCs in the performed PCA (with a large subset) describe processes that occur at a large number of cells in the data set. Events that might not correspond to these widespread behaviour such as the B event in Figure 5.6 are thus not represented in these PCs and are likely overlooked. By performing PCA at different subset sizes, the effects of this disadvantage of the PCA method could

be mitigated. In a future approach, it could be interesting to identify (spatial and temporal) subsets of interest through a PCA of a large data set, after which a PCA of these smaller-scale interesting subsets could yield more interpretable results which are not obscured by large-scale behaviour.

### Principal component influence overview

The false colour representation of the loading corresponding to the first three (combined) principal components provides a good insight into the spatial distribution of areas with similar range change time series. The heterogeneous distribution of colours on the lateral moraines indicate that these objects are subject to processes that have different behaviour in time such as the red zones corresponding to linear behaviour or the blue zones corresponding to sudden change around the two heavy precipitation events. The patterns in the visualisation show the potential for classification or clustering of this 4D spatiotemporal dataset based on PCA or other time series-derived features. Areas of constant colour are visible in the image, which indicates that rasters in these cells show similar range changes over time. Furthermore, with the knowledge of what time behaviour corresponds to the colours represented in the false colour image, this visualisation provides a lot of interpretable information which can be used to identify interesting areas to further analysis using their full time series data. A disadvantage of this visualisation is the relative loading magnitude used for the colour correspondence. As a result, negative and positive loading magnitudes are represented by the same colour intensity, limiting the distinction between areas of erosion and areas of deposition in this visualisation. The original PC loading images can be used to properly show this distinct.

### Comparing 2020 and 2022 principal components

The results of a PCA on the 2020 4D spatiotemporal data set are provided in Section 5.2.3. The PCs seem to show similar processes in 2020 and 2022. The actual PC where these processes can be identified might differ. The distribution of the first 2020 PC loading, as well as the scores, are very similar to the first PC of the 2022 data. This is as expected, as some of the processes linked to patterns in the first PC, such as ice melting, likely occur every summer. Like in 2022, some patterns of erosion (positive loading) above deposition (negative loading) areas are visible on and around the lateral moraine at  $\phi = 168^\circ$  and at the gully at  $\phi = 208^\circ$ . The third PC scores show a very clear step change at the end of August. Again, patterns of erosion above deposition are visible around the lateral moraines, around gullies as well as around the meltwater stream. Between the two scans before and after the PC scores change event, around 70mm of precipitation fell within 2 days ("Hintereneis station precipitation data", 2022), likely causing the geomorphological processes such as sheet erosion visible in the leftmost lateral moraine in Figure 5.22. In the right lower corner of this image, a deposition zone of a landslide can also be observed. The patterns found in the PCs of the 2020 4D spatiotemporal dataset are similar to the ones obtained in 2022, demonstrating that repetition of this method on a similar dataset yields similar results. As desired, the dates of the sudden change in the PC scores are different for the two different datasets as the weather events linked to these events do not occur on the same dates in the two different years.

### Comparison to clustering and segmentation methods

Recent studies utilising 4D spatiotemporal data from PLS systems aim to analyse surface deformations beyond a pairwise comparison. Among these methods is clustering based on time series-derived features by Kuschnerus et al. (Kuschnerus et al., 2021b) and Winiwarter et al. (Winiwarter et al., 2022). A study by Anders et al. (Anders et al., 2020) developed a new spatial and temporal segmentation method referred to as 4D objects by change which creates segments in space and time based on similarity in the temporal domain. Comparable to approaches in these studies, applying the PCA method on a 4D spatiotemporal dataset allows the isolation of similarly behaving locations. However, some traits of PCA are different from the above-mentioned methods. A PC describes a relation, which is responsible for a fraction of the variance in the dataset. Per PC this relation is expressed in the spatial and temporal domain of the dataset. Therefore, unlike the segments or clusters, a PC does not isolate a subset of the dataset but describes for all sampled locations, a part of its total time series signal. An advantage of the PCA method is that potentially, superimposed processes could be isolated and described over constant spatial and temporal domains, for example, the purple zones on the lateral moraine in Figure 5.18 indicate correspondence to the linear range change behaviour of the first PC, as well as a sudden change in one or both of the events of the third PC, showcasing isolation of two

superimposed types of change at these raster cells. A disadvantage of the PCA method is the fact that the events causing the largest variance in the dataset are high magnitude behaviour whose relations span a large fraction of the total domain. This limits the possibility of identifying local trends or behaviour in the dataset, which for example would be interesting when identifying pre-failure deformations before a rockfall event, which would be of a much smaller scale than the rockfall event itself and likely would end up spread out over several high order PCs if a large dataset is used. In this case, the 4D objects by change presented by Anders et al. (Anders et al., 2020) would be a more fitting method as the creation of a segment isolating a pre-failure deformations spatial and temporal extent is not influenced by other processes represented in the dataset. Compared to the other described methods, the PCA method as utilised in this thesis stands out in its ability to describe large-scale dependencies in spatiotemporal data but is less capable of isolating change behaviour of small spatial and temporal extent compared to the input dataset.

Little knowledge on the dataset is required beforehand, when applying PCA compared to other methods, as no additional input except for the data is required for the computation of PCs. For the K-means and agglomerative clustering methods in (Kuschnerus et al., 2021b), and the Gaussian mixed model clustering in (Winiwarter et al., 2021), the number of clusters must be defined before the clustering is performed. Therefore, the application of the PCA method is fitting for data for which no understanding of the (amount of) different captured processes is yet achieved. However, due to the aforementioned obscuring of small scale events, the PCA method does not necessarily provide a proper insight into the amount of processes. When using a Kalman filtering (Winiwarter et al., 2021) or temporal smoothing (Anders et al., 2020), knowledge on the process and measurement noise are required. Due to the complex processes contributing to measurement errors of the IHE PLS system, no proper model of the data noise is available, and therefore, the PCA is not performed on a Kalman filtered or temporally smoothed data set. Consequently, fractions of the signal used as input for the PCA originate from noise and errors and thus, fractions of the PCs will represent noise processes and errors.

### **Applicability in a different situation**

Applying the PCA method on the observations of the IHE PLS system, provided insights into the different types of geomorphological processes that occur in the observed area. Especially the processes causing large variance in the dataset can be identified using this method. Furthermore, spatial correlations are well highlighted using this method. Therefore, the PCA method could be of interest for data of areas where spatial dependencies are expected for the topographical change. In this research, for instance, this is the case for gravitational displacements of material, which are deposited at lower elevations. At a sandy beach, which is also observed by a PLS system, processes of interest could be the redistribution of sand around storm events, as mentioned by Vos et al. (Vos et al., 2017). In this case, PCA could potentially highlight locations and corresponding temporal behaviour of sand redistribution over the storm event, as well as the movement of sand during the restoration of the coast after the storm event. Applications of the PCA method to data containing vegetated areas in the data, as in the case of (Campos et al., 2021) likely do not provide insights into the data. In this case, depending on vegetation type, the variance in the dataset might be largely originating from high movement of vegetation at lower temporal scales than the PLS scan time. Furthermore, the current PCA method requires a rasterized representation of a 3D scene, which might not be straightforward to create for vegetated areas. This requirement also limits the use of the current PCA method on PLS data of scenes that can not be properly represented by a continuous surface, such as forests or urban areas, which contain a high variation in incidence angles of the surfaces. If this is the case, then the variance in the dataset will likely be dominated by slight changes or misalignments around areas of discontinuity or unfavourable incidence angles in the rasterised data, such as occurs around the gully edges in the IHE PLS data (as discussed in Section 4.2.2).

## **6.5. Potential of the IHE laser scanner for observing geomorphological processes**

By analysing the data captured by the IHE PLS system, multiple geomorphological processes are identified. Several objects in the view of this scanning system could be subject to further research potentially quantifying the changes of these objects. The lateral moraines as seen in the area used for PCA (indicated in yellow in Figure 3.7) are well captured by the scanning system. The angle of

incidence at most locations on these objects is favourable compared to other objects in the observed area. Furthermore, the topographical changes of these objects are of high magnitude compared to the magnitude of the measurement uncertainty. The PLS observations of these moraines could provide information on the erosion rates and processes of lateral moraines and their dependence on different factors such as temperature, precipitation events, or slope angles. The creation of a sediment budget for these features might be obstructed by the large influence of subsurface ice. However, for some locations this influence might be small and using an approach similar to (Altmann et al., 2020), utilizing Differences of Digital elevation models, could provide insights into the inputs of lateral moraines to mountain streams under different conditions. Although some areas are obscured, the gullies are another object which could be subject to further analysis. In the data of the PLS system, it can be seen that erosion occurred in these gullies over heavy precipitation events, leading to deposition underneath these objects. Again, the availability of precipitation and temperature data from a nearby station could provide insights into different factors causing gully erosion processes. Another interesting feature is the meltwater stream as discussed in Section 2.1. This stream causes erosion and deposition around its margins, which can be observed using the PLS system.

# 7

## Conclusions and recommendations

In this chapter, the conclusions to the results of this studies are presented. Following the conclusions, a number of recommendations are presented.

### 7.1. Conclusions

The aim of this research is to identify the different processes driving topographical change in the proglacial area adjacent to the Hintereisferner using a permanent laser scanning setup. Given the research questions, the following is concluded:

#### **Which geomorphological processes can be distinguished using the PLS setup?**

Various geomorphological processes are identified. Some examples include: sheet erosion and resulting deposition of material on lateral moraines, transport of material from gullies to lateral moraines caused by debris flows, and displacement of sediments by proglacial streams. By combining the PLS observations with webcam images, and meteorological data from nearby weather stations, the geomorphological processes linked to observed surface elevation changes can be estimated.

#### **At what (spatio-temporal) scales can geomorphological processes be identified?**

To identify geomorphological processes, spatial, as well as temporal relations must be assessed. In a range image, in order to assess spatial relations of surface change, these changes must span multiple cells. The cell size in the used range images correspond to surface areas in the decimeter scale, depending on object distance and geometry. Therefore, the smallest spatial scale at which geomorphological processes are identified is in the meter range. The temporal scale at which these processes are identified is dependent on the spatial scale of the process, and is at lowest on a day to day change scale, which corresponds to the observation frequency.

#### **How can uncertainty assessment of PLS data be incorporated in the identification of geomorphological processes?**

The uncertainty of the PLS system is expected to be around a decimeter at locations on the hillslope in favourable conditions, and this uncertainty is dependent on the stability of the scanner, viewing geometry, and atmospheric conditions. Therefore, the uncertainty of PLS data is heterogeneous over the observed area. At locations of unfavorable viewing geometry, range observations may differ by a few meters from scan to scan due to misalignment. A masking of these areas ensures these range changes are not linked to surface elevation change.

#### **How can multiple observations be combined to decrease the limit of detection and detect smaller surface changes?**

By utilizing PCA, patterns of similar change can be identified. By interpreting the patterns that result from this method, range changes of magnitudes below the uncertainty of a single observation are identified. Temporal and spatial means of the observations could not provide any insights into sub decimeter changes due to systematic errors likely caused by the registration method.

**How can range images be used to analyse surface change?**

Range images provide a good alternative to represent the laser scanning observations in a rasterised format in the case of repeated observations from a constant position, if no trivial plane exist along which to rasterise the observations. A range image registration method is developed. This method allows registration of multiple range images, such that each cell corresponds to a constant viewing angle, and one can analyse differences of range images. These difference of range images provide a good insight in the distribution of surface elevation change. Care must be taken when linking range change magnitudes to surface elevation change because this relation is very dependent on viewing geometry. The raster format of range images allows for straightforward application of convolutional and statistical methods such as computing neighborhood means, or performing a PCA.

**7.2. Recommendations**

This research focused mostly on the identification of surface elevation changes. However, the PLS setup also allows for a quantitative analysis of the changes occurring in the observed area.

In order to provide with more confidence the exact geomorphological processes that caused surface elevation change in the area of interest, a more elaborate analysis on the conditions surrounding the elevation change events should be performed.

Different data sources should be considered in order to investigate the effect of the low magnitude surface elevation change that is observed by the PLS system at the intergully slopes. With more precise measurements of surface elevation in these regions, it can be determined whether these observed changes are an error or actual surface elevation change is occurring.

The creation of a model for conversion of range observations to change in the local surface normal direction could, together with a model for ground sampling distance estimation, provide a basis for scaling, creating a more balanced representation of surface elevation changes in the dataset used for PCA.

An iterative approach in which PCA is performed at increasingly smaller subsets of the total data set might provide more detailed insights in smaller scale processes occurring at interesting locations.

The IHE PLS system combined with the webcams and nearby meteorological stations could provide valuable data for research on the relation between meteorological conditions and geomorphological activity.

# Bibliography

- Abedinia, A., Hahn, M., & Samadzadegan, F. (2008). An investigation into the registration of lidar intensity data and aerial images using the sift approach. *International Archives of Photogrammetry and Remote Sensing*, 37 (Part B1), 169–175.
- Altmann, M., Piermattei, L., Haas, F., Heckmann, T., Fleischer, F., Rom, J., Betz-Nutz, S., Knoflach, B., Müller, S., Ramskogler, K., et al. (2020). Long-term changes of morphodynamics on little ice age lateral moraines and the resulting sediment transfer into mountain streams in the upper kauner valley, Austria. *Water*, 12(12), 3375. <https://doi.org/10.3390/w12123375>
- Anders, K., Winiwarter, L., Lindenbergh, R., Williams, J. G., Vos, S. E., & Höfle, B. (2020). 4d objects-by-change: Spatiotemporal segmentation of geomorphic surface change from lidar time series. *ISPRS Journal of Photogrammetry and Remote Sensing*, 159, 352–363. <https://doi.org/10.1016/j.isprsjrs.2019.11.025>
- Ballantyne, C. K. (2002). Paraglacial geomorphology. *Quaternary Science Reviews*, 21(18-19), 1935–2017. [https://doi.org/10.1016/S0277-3791\(02\)00005-7](https://doi.org/10.1016/S0277-3791(02)00005-7)
- Besl, P. J., & McKay, N. D. (1992). A method for registration of 3d shapes. *IEEE Transactions on Pattern Analysis and Machine Intelligence*, 14, 239–254. <https://doi.org/10.1117/12.57955>
- Betz, S., Croce, V., & Becht, M. (2019). Investigating morphodynamics on little ice age lateral moraines in the Italian Alps using archival aerial photogrammetry and airborne lidar data. *Zeitschrift für Geomorphologie*, 231–247. <https://doi.org/10.1127/zfg/2019/0629>
- Birch, K., & Downs, M. (1993). An updated Edlén equation for the refractive index of air. *Metrologia*, 30(3), 155. <https://doi.org/10.1088/0026-1394/30/3/004>
- Bollmann, E., Sailer, R., Briese, C., Stoetter, J., & Fritzmann, P. (2011). Potential of airborne laser scanning for geomorphologic feature and process detection and quantifications in high alpine mountains. *Zeitschrift für Geomorphologie, Supplementary Issues*, 83–104. <https://doi.org/10.1127/0372-8854/2011/0055S2-0047>
- Campos, M. B., Litkey, P., Wang, Y., Chen, Y., Hyyti, H., Hyyppä, J., & Puttonen, E. (2021). A long-term terrestrial laser scanning measurement station to continuously monitor structural and phenological dynamics of boreal forest canopy. *Frontiers in Plant Science*, 11, 606–752. <https://doi.org/10.3389/fpls.2020.606752>
- Carrivick, J. L., & Heckmann, T. (2017). Short-term geomorphological evolution of proglacial systems. *Geomorphology*, 287, 3–28. <https://doi.org/10.1016/j.geomorph.2017.01.037>
- Chao, B., & Liao, J. (2019). Gravity changes due to large earthquakes detected in GRACE satellite data via empirical orthogonal function analysis. *Journal of Geophysical Research: Solid Earth*, 124(3), 3024–3035. <https://doi.org/10.1029/2018JB016862>
- Collins, B. D., & Stock, G. M. (2016). Rockfall triggering by cyclic thermal stressing of exfoliation fractures. *Nature Geoscience*, 9(5), 395–400. <https://doi.org/10.1038/ngeo2686>
- Curry, A., Cleasby, V., & Zukowskyj, P. (2006). Paraglacial response of steep, sediment-mantled slopes to post-'little ice age' glacier recession in the central Swiss Alps. *Journal of Quaternary Science: Published for the Quaternary Research Association*, 21(3), 211–225. <https://doi.org/10.1002/jqs.954>
- Demšar, U., Harris, P., Brunsdon, C., Fotheringham, A. S., & McLoone, S. (2013). Principal component analysis on spatial data: An overview. *Annals of the Association of American Geographers*, 103(1), 106–128. <https://doi.org/10.1080/00045608.2012.689236>

- Draebing, D., Mayer, T., Jacobs, B., & McColl, S. T. (2022). Alpine rockwall erosion patterns follow elevation-dependent climate trajectories. *Communications Earth & Environment*, 3(1), 1–12. <https://doi.org/10.1038/s43247-022-00348-2>
- Dusik, J.-M., Neugirg, F., & Haas, F. (2019). Slope wash, gully erosion and debris flows on lateral moraines in the upper kaunertal, austria. *Geomorphology of proglacial systems* (pp. 177–196). Springer. [https://doi.org/10.1007/978-3-319-94184-4\\_11](https://doi.org/10.1007/978-3-319-94184-4_11)
- Fischer, L., Kääb, A., Huggel, C., & Noetzi, J. (2006). Geology, glacier retreat and permafrost degradation as controlling factors of slope instabilities in a high-mountain rock wall: The monte rosa east face. *Natural Hazards and Earth System Sciences*, 6(5), 761–772. <https://doi.org/10.5194/nhess-6-761-2006>
- Fischler, M. A., & Bolles, R. C. (1981). Random sample consensus: A paradigm for model fitting with applications to image analysis and automated cartography. *Communications of the ACM*, 24(6), 381–395. <https://doi.org/10.1145/358669.358692>
- Gischig, V. S., Moore, J. R., Evans, K. F., Amann, F., & Loew, S. (2011). Thermomechanical forcing of deep rock slope deformation: 1. conceptual study of a simplified slope. *Journal of Geophysical Research: Earth Surface*, 116(F4). <https://doi.org/10.1029/2011JF002007>
- Guerin, A., Abellán, A., Matasci, B., Jaboyedoff, M., Derron, M.-H., & Ravanel, L. (2017). Brief communication: 3-d reconstruction of a collapsed rock pillar from web-retrieved images and terrestrial lidar data—the 2005 event of the west face of the drus (mont blanc massif). *Natural Hazards and Earth System Sciences*, 17(7), 1207–1220. <https://doi.org/10.5194/nhess-17-1207-2017>
- Hackel, T., Wegner, J. D., & Schindler, K. (2016). Fast semantic segmentation of 3d point clouds with strongly varying density. *ISPRS annals of the photogrammetry, remote sensing and spatial information sciences*, 3, 177–184. <https://doi.org/10.5194/isprs-annals-III-3-177-2016>
- Heckmann, T., & Morche, D. (2019). *Geomorphology of proglacial systems landform and sediment dynamics in recently deglaciated alpine landscapes*. Springer. <https://doi.org/https://doi.org/10.1007/978-3-319-94184-4>
- Hintereneis station precipitation data*. (2022). Department of Atmospheric and Cryospheric sciences, University Innsbruck. <https://acinn-data.uibk.ac.at/pages/station-hintereis.html>
- Im hinteren eis station precipitation data*. (2022). Department of Atmospheric and Cryospheric sciences, University Innsbruck. <https://acinn-data.uibk.ac.at/station/82/RAWDATA/>
- Kaiser, H. F. (1958). The varimax criterion for analytic rotation in factor analysis. *Psychometrika*, 23(3), 187–200. <https://doi.org/10.1007/BF02289233>
- Kang, Z. (2008). Automatic registration of terrestrial point cloud using panoramic reflectance images. *XXI ISPRS Congress, Commission I-VIII, 3-11 July 2008, Beijing, China*.
- Knoflach, B., Tussetschläger, H., Sailer, R., Meißl, G., & Stötter, J. (2021). High mountain rockfall dynamics: Rockfall activity and runout assessment under the aspect of a changing cryosphere. *Geografiska Annaler: Series A, Physical Geography*, 103(1), 83–102. <https://doi.org/10.1080/04353676.2020.1864947>
- Kuschnerus, M., Schröder, D., & Lindenbergh, R. (2021a). Environmental influences on the stability of a permanently installed laser scanner. *International Archives of the Photogrammetry, Remote Sensing and Spatial Information Sciences*, 43(B2-2021), 745–752. <https://doi.org/https://doi.org/10.5194/isprs-archives-XLIII-B2-2021-745-2021>
- Kuschnerus, M., Lindenbergh, R., & Vos, S. (2021b). Coastal change patterns from time series clustering of permanent laser scan data. *Earth Surface Dynamics*, 9(1), 89–103. <https://doi.org/10.5194/esurf-9-89-2021>
- Larson, M., Hanson, H., Kraus, N. C., & Newe, J. (1999). Short-and long-term responses of beach fills determined by eof analysis. *Journal of waterway, port, coastal, and ocean engineering*, 125(6), 285–293. [https://doi.org/10.1061/\(ASCE\)0733-950X\(1999\)125:6\(285\)](https://doi.org/10.1061/(ASCE)0733-950X(1999)125:6(285))

- Lato, M. J., Hutchinson, D. J., Gauthier, D., Edwards, T., & Ondercin, M. (2015). Comparison of airborne laser scanning, terrestrial laser scanning, and terrestrial photogrammetry for mapping differential slope change in mountainous terrain. *Canadian Geotechnical Journal*, *52*(2), 129–140. <https://doi.org/10.1139/cgj-2014-0051>
- Lay, D., Lay, S., & McDonald, J. (2015). *Linear algebra and its applications*. Pearson Education.
- Lowe, D. G. (1999). Object recognition from local scale-invariant features. *Proceedings of the seventh IEEE international conference on computer vision*, *2*, 1150–1157. <https://doi.org/10.1109/ICCV.1999.790410>
- McColl, S., & Draebing, D. (2019). Rock slope instability in the proglacial zone: State of the art. *Geomorphology of proglacial systems*, 119–141. [https://doi.org/https://doi.org/10.1007/978-3-319-94184-4\\_8](https://doi.org/https://doi.org/10.1007/978-3-319-94184-4_8)
- McColl, S. T., & Davies, T. R. (2013). Large ice-contact slope movements: Glacial buttressing, deformation and erosion. *Earth Surface Processes and Landforms*, *38*(10), 1102–1115. <https://doi.org/10.1002/esp.3346>
- North, G. R., Bell, T. L., Cahalan, R. F., & Moeng, F. J. (1982). Sampling errors in the estimation of empirical orthogonal functions. *Monthly weather review*, *110*(7), 699–706. [https://doi.org/10.1175/1520-0493\(1982\)110<0699:SEITEO>2.0.CO;2](https://doi.org/10.1175/1520-0493(1982)110<0699:SEITEO>2.0.CO;2)
- Porter, P. R., Smart, M. J., & Irvine-Fynn, T. D. (2019). Glacial sediment stores and their reworking. *Geomorphology of proglacial systems* (pp. 157–176). Springer. [https://doi.org/10.1007/978-3-319-94184-4\\_10](https://doi.org/10.1007/978-3-319-94184-4_10)
- Pörtner, H.-O., Roberts, D. C., Masson-Delmotte, V., Zhai, P., Tignor, M., Poloczanska, E., Mintenbeck, K., Nicolai, M., Okem, A., Petzold, J., et al. (2019). IPCC special report on the ocean and cryosphere in a changing climate. *IPCC Intergovernmental Panel on Climate Change: Geneva, Switzerland*, *1*(3). <https://doi.org/10.1017/9781009157964>
- Prantl, H., Nicholson, L., Sailer, R., Hanzer, F., Juen, I. F., & Rastner, P. (2017). Glacier snowline determination from terrestrial laser scanning intensity data. *Geosciences (Switzerland)*, *7*, 60. <https://doi.org/10.3390/geosciences7030060>
- Riegl. (2014). *3d terrestrial laser scanner rieg1 vz-4000 rieg1 / vz-6000 general description and data interfaces*. Version 03 / 09 CE.
- Sailer, R., Rutzinger, M., Rieg, L., & Wichmann, V. (2014). Digital elevation models derived from airborne laser scanning point clouds: Appropriate spatial resolutions for multi-temporal characterization and quantification of geomorphological processes. *Earth Surface Processes and Landforms*, *39*, 272–284. <https://doi.org/10.1002/esp.3490>
- Shen, Y., Lindenbergh, R., & Wang, J. (2017). Change analysis in structural laser scanning point clouds: The baseline method. *Sensors (Switzerland)*, *17*(1), 26. <https://doi.org/10.3390/s17010026>
- Smith, M. W., Carrivick, J. L., & Quincey, D. J. (2016). Structure from motion photogrammetry in physical geography. *Progress in Physical Geography*, *40*, 247–275. <https://doi.org/10.1177/0309133315615805>
- Soudarissanane, S., Lindenbergh, R., Menenti, M., & Teunissen, P. (2011). Scanning geometry: Influencing factor on the quality of terrestrial laser scanning points. *ISPRS Journal of Photogrammetry and Remote Sensing*, *66*, 389–399. <https://doi.org/10.1016/j.isprsjprs.2011.01.005>
- Umeyama, S. (1991). Least-squares estimation of transformation parameters between two point patterns. *IEEE Transactions on Pattern Analysis & Machine Intelligence*, *13*(04), 376–380. <https://doi.org/10.1109/34.88573>
- Vehling, L., Baewert, H., Glira, P., Moser, M., Rohn, J., & Morche, D. (2017). Quantification of sediment transport by rockfall and rockslide processes on a proglacial rock slope (kaunertal, austria). *Geomorphology*, *287*, 46–57. <https://doi.org/10.1016/j.geomorph.2016.10.032>

- Virtanen, P., Gommers, R., Oliphant, T. E., Haberland, M., Reddy, T., Cournapeau, D., Burovski, E., Peterson, P., Weckesser, W., Bright, J., van der Walt, S. J., Brett, M., Wilson, J., Millman, K. J., Mayorov, N., Nelson, A. R. J., Jones, E., Kern, R., Larson, E., . . . SciPy 1.0 Contributors. (2020). SciPy 1.0: Fundamental Algorithms for Scientific Computing in Python. *Nature Methods*, *17*, 261–272. <https://doi.org/10.1038/s41592-019-0686-2>
- Voordendag, A., Goger, B., Klug, C., Prinz, R., Rutzinger, M., & Kaser, G. (2021). Automated and permanent long-range terrestrial laser scanning in a high mountain environment: Setup and first results. *ISPRS Annals of the Photogrammetry, Remote Sensing and Spatial Information Sciences*, *5*, 153–160. <https://doi.org/10.5194/isprs-annals-V-2-2021-153-2021>
- Voordendag, A., Goger, B., Klug, C., Prinz, R., Rutzinger, M., & Kaser, G. (2022). The stability of a permanent terrestrial laser scanning system - a case study with hourly scans. *The International Archives of the Photogrammetry, Remote Sensing and Spatial Information Sciences*, *XLIII-B2-2022*, 1093–1099. <https://doi.org/10.5194/isprs-archives-xliii-b2-2022-1093-2022>
- Vos, S., Anders, K., Kuschnerus, M., Lindenbergh, R., Höfle, B., Aarninkhof, S., & de Vries, S. (2022). A high-resolution 4d terrestrial laser scan dataset of the kijkduin beach-dune system, the netherlands. *Scientific Data*, *9*(1), 1–11.
- Vos, S., Lindenbergh, R., de Vries, S., Aagaard, T., Deigaard, R., & Fuhrman, D. (2017). Coastscan: Continuous monitoring of coastal change using terrestrial laser scanning. *Proceedings of Coastal Dynamics, 2017*, 1518–1528.
- Vosselman, G., & Maas, H.-G. (2010). *Airborne and terrestrial laser scanning*. Whittles publishing.
- Westoby, M., Brasington, J., Glasser, N., Hambrey, M., & Reynolds, J. (2012). 'structure-from-motion' photogrammetry: A low-cost, effective tool for geoscience applications. *Geomorphology*, *179*, 300–314. <https://doi.org/https://doi.org/10.1016/j.geomorph.2012.08.021>
- Wilks, D. S. (2011). Principal component (eof) analysis. *International geophysics* (pp. 519–562). Elsevier. <https://doi.org/https://doi.org/10.1016/B978-0-12-385022-5.00012-9>
- Williams, J. G., Rosser, N. J., Hardy, R. J., Brain, M. J., & Afana, A. A. (2018). Optimising 4-d surface change detection: An approach for capturing rockfall magnitude-frequency. *Earth Surface Dynamics*, *6*, 101–119. <https://doi.org/10.5194/esurf-6-101-2018>
- Winiwarter, L., Anders, K., & Höfle, B. (2021). M3c2-ep: Pushing the limits of 3d topographic point cloud change detection by error propagation. *ISPRS Journal of Photogrammetry and Remote Sensing*, *178*, 240–258. <https://doi.org/10.1016/j.isprsjprs.2021.06.011>
- Winiwarter, L., Anders, K., Schröder, D., & Höfle, B. (2022). Full 4d change analysis of topographic point cloud time series using kalman filtering. <https://doi.org/10.5194/esurf-2021-103>